Absolute Calibration and Characterization of the Multiband Imaging Photometer for *Spitzer*. II. 70 μm Imaging

Karl D. Gordon,[1] Charles W. Engelbracht,[1] Dario Fadda,[2] John Stansberry,[1] Stefanie Wachter,[2] Dave T. Frayer,[2] George Rieke,[1] Alberto Noriega-Crespo,[2] William B. Latter,[3] Erick Young,[1] Gerry Neugebauer,[1] Zoltan Balog,[1] Jeffrey W. Beeman,[4] Hervé Dole,[5] Eiichi Egami,[1] Eugene E. Haller,[4,6] Dean Hines,[7] Doug Kelly,[1] Francine Marleau,[2] Karl Misselt,[1] Jane Morrison,[1] Pablo Pérez-González,[1,8] Jeonghee Rho,[2] and Wm. A. Wheaton[2]

Received 2006 November 15; accepted 2007 April 16; published 2007 October 2

ABSTRACT. The absolute calibration and characterization of the Multiband Imaging Photometer for *Spitzer* (MIPS) 70 μm coarse- and fine-scale imaging modes are presented based on over 2.5 yr of observations. Accurate photometry (especially for faint sources) requires two simple processing steps beyond the standard data reduction to remove long-term detector transients. Point-spread function (PSF) fitting photometry is found to give more accurate flux densities than aperture photometry. Based on the PSF fitting photometry, the calibration factor shows no strong trend with flux density, background, spectral type, exposure time, or time since anneals. The coarse-scale calibration sample includes observations of stars with flux densities from 22 mJy to 17 Jy, on backgrounds from 4 to 26 MJy sr^{-1}, and with spectral types from B to M. The coarse-scale calibration is 702 ± 35 MJy sr^{-1} MIPS70^{-1} (5% uncertainty) and is based on measurements of 66 stars. The instrumental units of the MIPS 70 μm coarse- and fine-scale imaging modes are called MIPS70 and MIPS70F, respectively. The photometric repeatability is calculated to be 4.5% from two stars measured during every MIPS campaign and includes variations on all timescales probed. The preliminary fine-scale calibration factor is 2894 ± 294 MJy sr^{-1} MIPS70F^{-1} (10% uncertainty) based on 10 stars. The uncertainties in the coarse- and fine-scale calibration factors are dominated by the 4.5% photometric repeatability and the small sample size, respectively. The 5 σ, 500 s sensitivity of the coarse-scale observations is 6–8 mJy. This work shows that the MIPS 70 μm array produces accurate, well-calibrated photometry and validates the MIPS 70 μm operating strategy, especially the use of frequent stimulator flashes to track the changing responsivities of the Ge:Ga detectors.

1. INTRODUCTION

The Multiband Imaging Photometer for *Spitzer* (MIPS; Rieke et al. 2004) is the far-infrared imager on the *Spitzer Space Telescope* (*Spitzer*; Werner et al. 2004). MIPS images the sky in bands at 24, 70, and 160 μm. The absolute calibration of the MIPS bands is complicated by the challenging nature of removing the instrumental signatures of the MIPS detectors, as well as predicting the flux densities of calibration sources accurately at far-infrared wavelengths. This paper describes the

calibration and characterization of the 70 μm band. Companion papers provide the transfer of previous absolute calibrations to the MIPS 24 μm band (G. H. Rieke et al. 2007, in preparation), the 24 μm band calibration and characterization (Engelbracht et al. 2007), and 160 μm band calibration and characterization (Stansberry et al. 2007). Engelbracht et al. (2007) also present the MIPS stellar calibrator sample that is used for this paper. The calibration factors derived in these papers represent the official MIPS calibration and are due to the combined efforts of the MIPS Instrument Team (at the University of Arizona) and the MIPS Instrument Support Team (at the *Spitzer* Science Center).

The characterization and calibration of the MIPS 70 μm band is based on stellar photospheres. The repeatability of 70 μm photometry is measured from observations of two stars, at least one of which is observed in every MIPS campaign. The absolute calibration of the 70 μm band is based on a large network of stars observed in the standard coarse-scale photometry mode with a range of predicted flux densities and backgrounds. In addition to the coarse-scale observations, a small number of stars were observed in the fine-scale photometry mode to allow

---

[1] Steward Observatory, University of Arizona, Tucson, AZ.

[2] *Spitzer* Science Center, California Institute of Technology, Pasadena, CA.

[3] NASA *Herschel* Science Center, California Institute of Technology, Pasadena, CA.

[4] Materials Science Division, Lawrence Berkeley National Laboratory, Berkeley, CA.

[5] Institut d'Astrophysique Spatiale (IAS), Orsay, France.

[6] Department of Materials Science and Engineering, University of California, Berkeley, Berkeley, CA.

[7] Space Science Institute, Boulder, CO.

[8] Departamento de Astrofísica, Facultad de CC. Físicas, Universidad Complutense de Madrid, Madrid, Spain.

the coarse-scale calibration to be transferred to this mode. The observations used in this paper include both in-orbit checkout (IOC; MIPS campaigns R, V, X1, and W) and regular science operations (MIPS campaigns 1–29) with a cutoff date of 2006 March 3.

The goal of the calibration is to transform measurements in instrumental units to instrument-independent physical units. The goal of the characterization is to determine whether the calibration depends on how the data are taken (e.g., exposure time, time since anneal) or characteristics of the sources being measured (e.g., flux density, background). The primary challenge for the 70 μm characterization and calibration is accurately correcting the detector transients associated with Ge:Ga detectors. The standard reduction steps are detailed in Gordon et al. (2005), but extra steps to achieve accurate photometry with the highest possible signal-to-noise ratio (S/N) for point sources are needed and discussed in this paper. Accurate calibration and high sensitivity are important at 70 μm, as they enable a number of science investigations, including the detection and study of cold disks around stars (e.g., Kim et al. 2005; Bryden et al. 2006), imaging of warm dust in galaxies (e.g., Calzetti et al. 2005; Dale et al. 2005; Gordon et al. 2006), and investigation of faint, redshifted galaxies (e.g., Dole et al. 2004a; Frayer et al. 2006a).

2. DATA

The 70 μm calibration program is based on stars with spectral types from B to M, predicted flux densities from 22 mJy to 17 Jy, and predicted backgrounds from 4 to 26 MJy sr^{-1} (Engelbracht et al. 2007). The observations were carried out in photometry mode with 3.15–10.49 s individual image exposure times and a range of total exposure times from ~50 to ~560 s. The majority of the observations were performed in standard coarse-scale photometry mode, with a few done in the standard fine-scale photometry mode. The coarse- and fine-scale photometry modes are also referred to as the wide- and narrow-field photometry modes.

The coarse-scale mode samples the 18″ FWHM 70 μm point-spread function (PSF) with 9.85″ pixels. The minimum coarse-scale photometry mode observation consists of 12 images of the target and four images where the internal calibration stimulator is flashed (see Fig. 2 of Gordon et al. 2005). The target point source is dithered around the central part of the good half of the 70 μm array so that the source is on different pixels for each of the 12 image exposures. The stimulator flashes are used to remove the responsivity variations in the Ge:Ga detectors by dividing each image exposure by an interpolated stimulator flash. This division converts the raw DN s^{-1} units to fractions of the stimulator flash amplitude (also measured in DN s^{-1} units), which are termed MIPS70 units. These MIPS70 units are surface brightness units, as the varying pixel size across the array has been normalized out due to the division by the stimulator flash. Read-

ers should refer to Rieke et al. (2004) and Gordon et al. (2005) for the details on how MIPS data are taken and reduced. The maximum image exposure time is 10.49 s; thus, longer total exposures on a source are acquired by repeating the minimum set of images described above.

The fine-scale mode samples the same 70 μm PSF with 5.24″ pixels and is designed for detailed studies of source structure. The dithering strategy is different for fine-scale mode, in which source-background pairs of images are acquired instead of dithering the source around the array. The minimum fine-scale photometry mode observation consists of eight source-background pairs of images, four stimulator images, and two dedicated stimulator background images. The data reduction is the same as for the coarse-scale mode, and thus, the resulting raw units of the images are also fractions of the stimulator flash and are termed MIPS70F units. These units are different than the MIPS70 units due to the change in the optical train used.

The coarse-scale observations were extensive and motivated to check nonlinearities versus flux density, background, exposure time, etc. The fine-scale observations were done to transfer the coarse-scale calibration to the fine scale. The coarse-scale and scan map modes share the same optical train and only differ in the dithering strategy; thus, the coarse-scale photometry calibration should apply to the scan map mode observations.

2.1. Data Reduction

Each observation was reduced through the MIPS Data Analysis Tool (DAT, ver. 3.06, Gordon et al. 2005). The resulting mosaics of this default processing are shown in Figures 1a and 1d for two point sources observed in coarse-scale mode. It is possible to improve the detection of point sources taken in photometry mode by utilizing the redundancy of the observations to remove residual instrumental signatures. These residual signatures arise because the stimulator flashes calibrate the fast response of the detectors well, but there is a drift between the fast and slow response of the detectors (Haegel et al. 2001; Gordon et al. 2005). In coarse-scale mode, point sources are dithered around the array to ensure that their signals are in the well-calibrated fast response. The dithering does not put the background signal in the fast response, and, as the sky level is roughly equal at the different dither positions, the background is in the slow-response regime. As an accurate measurement of the background is essential for good photometry, the drifting background needs to be corrected by two additional steps. The extra steps are designed not to introduce biases into the data based on source flux density while reducing the residual instrumental signatures.

The largest portion of the drift is seen to be in common among pixels in the same column. This is not surprising, as columns represent a common strip of detector material (Young et al. 1998). The column offset can be removed easily for observations of isolated point sources by subtracting the median
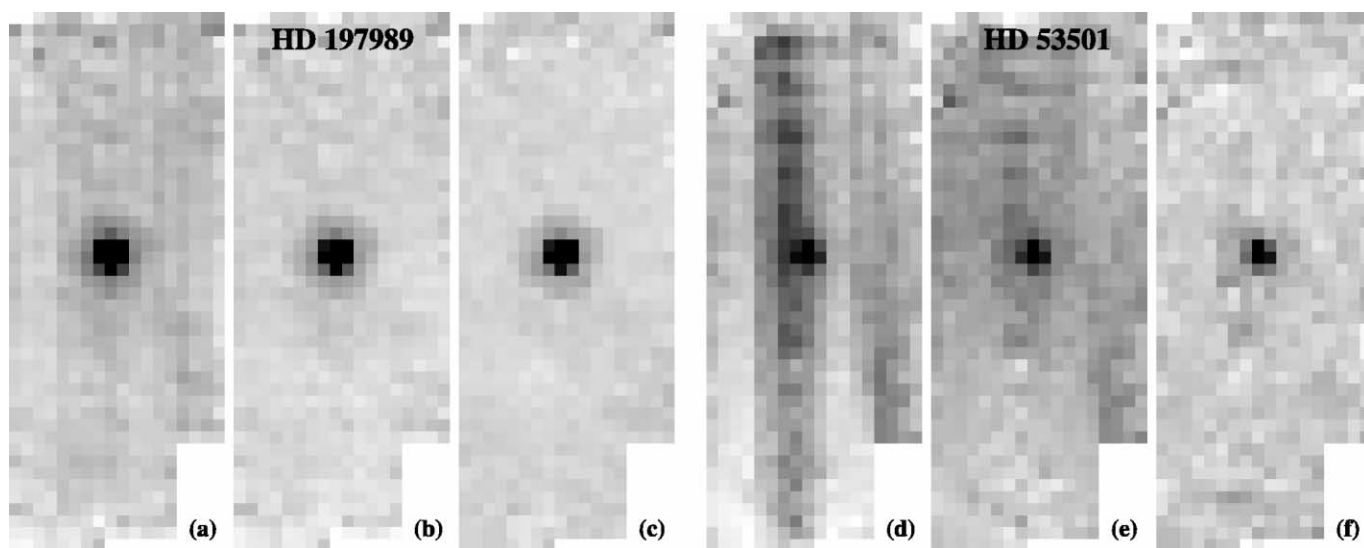
Fig. 1.—Mosaics of coarse-scale observations of two stars of different brightness shown with (*a*, *d*) default reductions, (*b*, *e*) column mean subtraction, and (*c*, *f*) column mean subtraction and time filtering. The two stars are HD 197989 (AOR key 13590784, flux density = 787 mJy) and HD 53501 (AOR key 13641984, flux density = 135 mJy). The HD 197989 images are displayed with a linear stretch that ranges (*a*) from 0.022 to 0.05, (*b*) from -0.005 to 0.025, and (*c*) from -0.005 to 0.0025. The HD 53501 images are displayed with a linear stretch that ranges (*d*) from 0.009 to 0.025, (*e*) from -0.005 to 0.01, and (*f*) from -0.002 to 0.008. The images and ranges are all given in MIPS70 units.

of the column. The median of each column is computed after excluding a region centered on the source with a diameter of 9 pixels ($\sim 89''$) to ensure that the resulting correction is not biased by the source. The column-subtracted data are shown in Figures 1*b* and 1*e*. A smaller but still significant background drift seen as array-dependent structure is still present after this correction. This smaller residual instrument signature can be removed from each pixel by using a simple time filter. This time filter works by subtracting the mean value from a pixel of the previous and next 14 measurements of that pixel. To ensure that this mean value is not biased by the presence of the source itself, all measurements of the source within a spatial radius of 4.5 pixels, as well as the current, previous, and next measurements, are not used in computing the mean value. The mean is computed after excluding all the pixels $>4\,\sigma$ from the median (sigma clipping). The time filter only uses data taken on a particular source, which means that the time filtering is less accurate at the beginning and end of the observation set. This time filtering with constraints was optimized to minimize the background noise. The result is shown in Figures 1*c* and 1*f*. From the two examples shown in Figure 1, it is clear that the importance of these extra processing steps increases with decreasing source flux density.

Unlike coarse-scale photometry mode, in which the large field of view provides sufficient area for background estimates, the reduced field of view of the find-scale mode requires that the point source be chopped off the array. This simplifies the extra processing to just subtracting the images taken in the off

positions from the on position images, which effectively removes the column offsets and smaller scale pixel-dependent drifts in the background.

2.2. Aperture Corrections

A necessary part of measuring the flux density of a point source using aperture photometry or point-spread function (PSF) fitting is an accurate PSF. The repeatability measurements on HD 163588 and HD 180711 provide the ideal opportunity to compare the STinyTim (Krist 2002) model of the MIPS 70 μm PSF to the coarse-scale observations. The repeated observations of these two stars allow for very high S/N observed PSFs to be constructed. All of the observations of these two stars taken after the final optimization of the array parameters (fifth and later MIPS campaigns) were mosaicked to produce two empirical PSFs. The fine-scale observed PSFs are from observations of the fine-scale calibration stars. The observed PSFs are compared with the STinyTim PSF for a $T = 10,000$ K blackbody in Figure 2. All stars in our calibration program have the same spectrum across the 70 μm band as the Rayleigh-Jeans tail of stellar spectra is being sampled. Thus, the PSF generated assuming a $T = 10,000$ K blackbody is a good representation of any star's PSF as long as it does not have an infrared excess.

As can be seen for both coarse and fine scales, the model PSF well represents the observed PSFs when the smoothing associated with the pixel sampling is applied. We have simu-
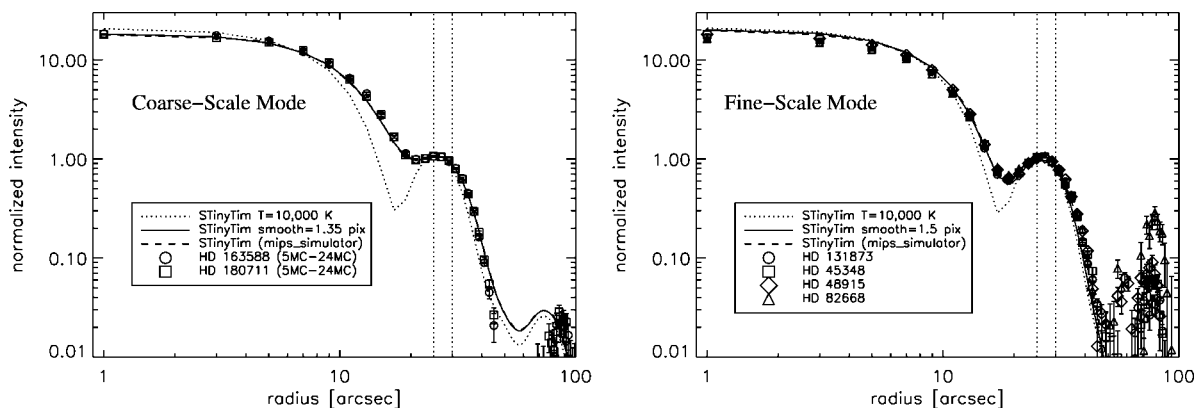
FIG. 2.—Radial profiles of the observed and model PSFs plotted for coarse-scale and fine-scale modes. The uncertainties on the observed PSFs are calculated from the standard deviation of the mean of the measurements in each measurement annulus. The PSF as predicted from STinyTim is shown, as well as two smoothed model PSFs. All the PSFs have been normalized to 1 between radii of 25″ and 30″ (between the vertical dotted lines) with the background determined from 100″–200″ for the coarse scale and 70″–100″ for the fine scale. In both plots, it is clear that the observed PSFs are well measured out to around 40″, where the PSF is about 1/1000 the brightness of the peak.

lated the pixel sampling smoothing with two different methods. The first method used uses the mips_simulator program, which produces simulated MIPS observations with the observed dithering using an input PSF. These simulated observations were mosaicked, using the same software that is used for the actual observations, to produce the mips_simulator PSF shown. The second method uses a simple boxcar smoothing function. The "smooth = 1.35 pix" and "smooth = 1.5 pix" PSFs are created by directly smoothing the STinyTim PSF with a square kernel with the specified width, where the pixel sizes are 9.85″ and 5.24″ for the coarse and fine scales, respectively. The close correspondence between the observed, mips_simulator, and directly smoothed PSFs means that accurate MIPS 70 μm PSFs can be generated from the STinyTim PSF smoothed with a simple square kernel.

The correspondence between the observed and STinyTim model PSFs was expected, as the MIPS 70 μm band should be purely diffraction limited. The 70 μm band has a bandwidth of ~19 μm, resulting in the PSF varying significantly between blue (peaking at wavelengths shorter than the band) and red (peaking at wavelengths longer than the band) sources. In addition to stellar sources, we have verified that STinyTim model PSFs describe the observed PSFs for sources with blackbody temperatures as low as 60 K using observations of asteroids and Pluto. Finally, no evidence for a blue or red leak at 70 μm was found, as the Fourier power spectra (Kirby et al. 1994) of blue (stellar) and red (ULIRG) PSFs were virtually identical. Having a valid model for the PSF allows for accurate, noiseless aperture corrections, as the total flux density is known from PSFs created with different source spectra.

The observed fine-scale PSFs do show disagreement in the core, where the model PSF is systematically higher. This is not surprising given that there are known flux density nonlinearities in the Ge:Ga detectors that are not corrected in the standard

data reduction and the fine-scale calibration stars are brighter than those observed in the coarse-scale mode. Characterization of these flux density nonlinearities is ongoing, but preliminary indications are that they are ~15% for point-source flux densities of ~20 Jy observed in the coarse-scale mode (see § 3.1). The coarse-scale observed PSFs do not show any systematic disagreement in the core, consistent with the use of fainter stars.

The aperture corrections were calculated by performing aperture photometry on square kernel–smoothed model PSFs. The model PSFs were computed for a $64' \times 64'$ field to ensure that the total flux of a point source was measured. The method for computing the aperture corrections is the same as used for measuring the calibration star flux densities used in this paper. The method does not account for partial pixels, but given that the model PSFs were computed with pixels 10 times smaller than the array pixel, size this is not expected to be an issue even for the smallest apertures considered in this paper. For the purposes of this paper, we use the radius = 35″ aperture (1.22 aperture correction) to minimize the sensitivity of the calibration to uncertainty in the aperture correction and centering errors. The aperture corrections for a small sample of object aperture and background annuli are given in Table 1 for three PSFs (T = 10,000, 60, and 10 K blackbodies). Three PSFs with different source spectra are given to emphasize the importance of using PSFs with the right source spectrum for accurate photometry.

2.3. Measurements

The photometry was measured with aperture photometry and PSF fitting for each observation of a calibration star. The aperture photometry was done with a circular aperture with a radius of 35″ and a sky annulus of 39″–65″. The PSF fitting was done with StarFinder (Diolaiti et al. 2000), which is ideally

TABLE 1
APERTURE CORRECTIONS

	RADIUS	BACKGROUND	PSF		
DESCRIPTION	(arcsec)	(arcsec)	$T = 10,000$ K	$T = 60$ K	$T = 10$ K
Coarse Scale					
Beyond second Airy ring	100	120–140	1.10	1.10	1.13
Beyond first Airy ring	35	39–65	1.22	1.24	1.48
2 × HWHM	16	18–39	2.04	2.07	2.30
Fine Scale					
Beyond second Airy ring	100	120–140	1.10	1.10	1.13
Beyond first Airy ring	35	39–65	1.21	1.22	1.47
2 × HWHM	16	18–39	1.93	1.94	2.16

suited for the well-sampled and stable MIPS PSFs. For the very brightest sources ($\gtrsim 3$ Jy), we progressively reduced the weight of core pixels in the PSF fitting as they increased in brightness above a threshold of 0.3 MIPS70. This produces more linear photometry for bright sources (see § 3.1), which is especially important for the 160 μm calibration (Stansberry et al. 2007). The flux densities measured with these two methods are listed in Tables 2 and 3. The aperture flux densities have had the aperture correction applied, and the PSF flux densities are naturally for an infinite aperture. In addition to the reported flux densities, S/N calculations are also reported. In the case of the aperture photometry, the S/N calculation is done using the noise in the sky annulus to determine both the uncertainty due to summing the object flux density, as well as subtracting the background. This S/N does not include the contribution from the photon noise of the source, as the gain of Ge:Ga detectors is not a well-defined quantity. In the case of the PSF photometry, the S/N calculation is done by the StarFinder program utilizing the empirical uncertainty image calculated from the repeated measurements of each point in the mosaic. Only measurements with S/N greater than 5 are reported in Tables 2 and 3. The columns in these tables give the star name, campaign of observation, AOR key (unique *Spitzer* observation identifier), exposure start time, individual exposure time, total exposure time, aperture flux density, S/N, PSF flux density, and S/N.

The measurements used in this paper were all reduced with the DAT and custom software based on the DAT results. Comparisons were done with measurements using data reduced with the *Spitzer* Science Center (SSC) pipeline and similar software available from the contributed software portion of the *Spitzer* Web site.[9] Note that the SSC pipeline reduced images are given in MJy sr^{-1} and must be divided by the applied flux conversion factor (given by the FITS header keyword FLUXCONV) to recover the instrumental MIPS70 or MIPS70F units. The result of this comparison is that the two methods produce equivalent results with a mean ratio of DAT to SSC aperture photometry for the full sample of 0.994 ± 0.037.

2.4. Flux Density Predictions

The predicted flux densities at 70 μm were derived from the 24 μm predictions presented by Engelbracht et al. (2007) using 24/70 μm colors derived from models. For each star, the ratio of the flux densities at the effective filter wavelengths of 23.675 and 71.42 μm was computed for the appropriate Kurucz (1979)[10] model (using a power-law interpolation) and a blackbody at the effective temperature of the star. The model ratio was taken to be the average of these two values, which typically differed by 1%–2%, and the uncertainty was taken to be the difference between them. The predicted flux densities at 24 μm were divided by this ratio to compute the 70 μm flux densities. The uncertainties on the flux density predictions were calculated by adding in quadrature the uncertainties in the 24 μm flux density and in the 24/70 μm color prediction. The average predicted backgrounds for the observations were estimated from *Spitzer* Planning Observations Tool (SPOT) with the uncertainties giving the range when each target is visible. The full sample of calibration stars covers a wide range of ecliptic and Galactic latitudes, providing a large range in backgrounds, but for any particular star the backgrounds vary by <30% for different dates of observation. The flux density predictions and background estimates are listed in Tables 4 and 5. These tables also give each star's spectral type, the average of the measured aperture and PSF flux densities, and their associated S/Ns. In addition, the average calibration factor determined using the aperture and PSF fitting measurements is given (see § 3.1).

The zero point of the 70 μm band at the effective filter wavelength of 71.42 μm is 0.778 ± 0.012 Jy in the G. H. Rieke et al. (2007, in preparation) system. It is important to note that the 70 μm calibration is based on stars (10,000 K blackbody). Thus, measuring accurate 70 μm flux densities for objects with different spectral energy distributions requires the use of the color corrections given in Stansberry et al. (2007).

---

[9] See http://ssc.spitzer.caltech.edu/archanaly/contributed/.

[10] Vizier Online Data Catalog, 6039 (R. L. Kurucz, 1993).

TABLE 2
COARSE-SCALE MEASUREMENTS

Name	Campaign[a]	AOR Key	Time[b] (s)	Exp. Time (s)	Total Time[c] (s)	Aperture Flux (MIPS70)	S/N	PSF Flux (MIPS70)	S/N
HD 002151	8MC	9806592	770,515,712	10.49	259.5	1.53E−01	20.4	1.62E−01	47.6
	10MC	10091520	773,862,336	3.15	77.7	1.52E−01	20.6	1.58E−01	42.5
	26MC	16276992	815,940,416	3.15	78.0	1.52E−01	22.9	1.52E−01	25.6
HD 002261	X1	7977216	753,515,520	3.15	78.3	7.15E−01	93.5	6.88E−01	58.3
HD 003712	11MC	11784448	775,613,056	3.15	78.1	7.11E−01	135.3	7.37E−01	70.2
HD 004128	16MC	12873216	786,539,520	3.15	78.2	6.98E−01	143.9	6.90E−01	63.6
HD 006860	12MC	11893504	777,752,832	3.15	78.5	3.04E+00	209.6	3.40E+00	96.6
HD 009053	11MC	11784960	775,614,464	3.15	78.2	8.85E−01	201.3	9.10E−01	78.0
HD 009927	11MC	11784704	776,018,752	3.15	78.3	2.93E−01	85.2	2.77E−01	49.6
	28MC	16619776	821,558,080	3.15	77.8	2.98E−01	79.8	2.94E−01	46.3
HD 012533	12MC	11893760	777,753,856	3.15	78.5	1.24E+00	189.0	1.30E+00	81.5
HD 012929	18MC	13113344	791,238,208	3.15	53.2	1.04E+00	144.7	1.08E+00	70.7
HD 015008	13MC	12064768	780,277,312	10.49	510.9	1.98E−02	9.2	1.36E−02	15.4
		12154368	780,623,616	10.49	511.0	1.82E−02	9.5	1.04E−02	10.4
		12154624	780,621,184	10.49	510.3	1.50E−02	9.4	1.31E−02	12.8
HD 018884	12MC	11894016	777,747,392	3.15	78.5	2.60E+00	268.4	2.89E+00	107.4
HD 020902	29MC	16868864	824,522,048	10.49	260.8	3.13E−01	87.3	3.02E−01	30.9
HD 024512	1MC	8358144	755,758,720	10.49	91.2	1.29E+00	175.2	1.36E+00	71.4
		8358400	755,759,040	3.15	52.6	1.47E+00	173.5	1.54E+00	74.6
	14MC	12197376	782,166,144	3.15	78.3	1.46E+00	211.6	1.52E+00	79.9
HD 025025	13MC	12063744	779,604,736	3.15	78.2	1.48E+00	223.5	1.55E+00	86.1
HD 029139	19MC	13315072	793,954,560	3.15	53.1	5.96E+00	174.9	7.87E+00	114.8
HD 031398	13MC	12064000	780,105,728	3.15	78.3	1.11E+00	176.1	1.20E+00	79.3
HD 032887	13MC	12064256	779,604,352	3.15	78.1	7.31E−01	172.4	7.25E−01	61.3
HD 034029	4MC	9059840	761,915,840	3.15	78.5	2.74E+00	331.2	2.91E+00	130.5
	13MC	12064512	780,235,008	3.15	78.5	2.69E+00	240.4	3.11E+00	108.1
HD 035666	9MC	9941248	772,043,584	10.49	510.9	2.07E−02	14.8	1.76E−02	16.8
	20MC	13478656	797,749,696	3.15	304.7	1.47E−02	7.0	1.76E−02	16.5
HD 036167	19MC	13308416	794,234,816	3.15	78.0	2.42E−01	27.5	2.34E−01	37.4
	29MC	16869120	825,753,280	10.49	259.9	2.72E−01	30.4	2.39E−01	35.8
HD 039425	R	7600896	753,649,280	3.15	78.1	3.52E−01	58.0	2.89E−01	14.7
HD 039608	12MC	11892992	777,732,992	10.49	510.8	3.09E−02	21.3	2.23E−02	24.8
	20MC	13479168	797,750,528	10.49	510.9	2.14E−02	12.4	2.02E−02	20.3
HD 042701	9MC	9941504	772,044,608	10.49	510.7	6.10E−02	43.8	3.18E−02	34.8
HD 045348	6MC	9459712	765,979,776	3.15	78.2	1.75E+00	317.7	1.84E+00	114.9
HD 048915	6MC	9458432	765,977,856	3.15	78.4	1.60E+00	246.8	1.68E+00	101.1
HD 050310	X1	7977984	753,518,784	3.15	78.0	4.13E−01	52.3	4.14E−01	41.0
		7979520	753,518,528	3.15	78.3	4.49E−01	61.7	4.28E−01	45.4
	21MC	13641472	800,741,248	3.15	78.4	4.45E−01	105.3	4.35E−01	51.9
HD 051799	R	7601152	753,649,664	3.15	71.5	4.09E−01	84.2	3.93E−01	44.0
	21MC	13641728	800,740,928	3.15	78.2	3.90E−01	113.9	3.79E−01	52.2
HD 053501	R	7601408	753,650,112	3.15	77.8	9.13E−02	13.4	8.35E−02	22.6
	X1	7977728	753,518,144	3.15	77.9	1.14E−01	15.6	1.00E−01	22.7
	21MC	13641984	800,744,576	3.15	78.2	9.84E−02	25.3	7.73E−02	31.1
HD 056855	19MC	13315328	793,945,152	3.15	53.1	1.61E+00	187.3	1.77E+00	85.3
HD 059717	15MC	12397824	784,145,600	3.15	78.3	8.89E−01	159.8	9.23E−01	76.9
HD 060522	20MC	13440768	797,687,296	3.15	52.8	4.54E−01	92.8	4.56E−01	42.1
HD 062509	15MC	12398080	784,147,584	3.15	78.6	1.56E+00	171.9	1.64E+00	93.7
HD 071129	3MC	8813312	759,211,520	3.15	78.4	3.12E+00	264.5	3.09E+00	86.7
	16MC	12873472	786,542,720	3.15	78.6	2.83E+00	201.5	3.33E+00	128.0
	28MC	16620032	821,426,816	3.15	78.5	2.75E+00	197.1	3.15E+00	120.7
	29MC	16868608	824,534,592	3.15	78.5	2.81E+00	204.9	3.03E+00	95.0
HD 080007	6MC	9459200	765,981,056	10.49	259.7	1.34E−01	38.4	1.23E−01	36.7
	19MC	13308672	794,194,496	3.15	78.1	1.42E−01	36.1	1.30E−01	37.6
HD 080493	21MC	13634304	800,483,200	3.15	78.3	1.02E+00	166.4	1.08E+00	78.6
		13642752	800,733,696	3.15	78.4	1.03E+00	195.9	1.06E+00	77.0
HD 081797	21MC	13634048	800,449,280	3.15	78.4	1.76E+00	212.0	1.86E+00	95.9
HD 082308	W	7966464	754,628,224	3.15	78.2	3.58E−01	43.2	2.68E−01	14.2
	21MC	13643264	800,736,128	3.15	78.1	3.25E−01	79.5	3.27E−01	51.0
HD 082668	7MC	9661952	768,555,648	3.15	78.1	9.61E−01	107.6	9.73E−01	61.5

TABLE 2 (*Continued*)

Name	Campaign[a]	AOR Key	Time[b] (s)	Exp. Time (s)	Total Time[c] (s)	Aperture Flux (MIPS70)	S/N	PSF Flux (MIPS70)	S/N
	10MC	10091264	773,861,824	3.15	78.1	9.13E−01	122.7	8.87E−01	58.1
HD 087901	W	7965440	754,625,728	3.15	78.0	1.05E−01	14.1	1.11E−01	28.1
	7MC	9661440	767,950,848	10.49	261.1	1.02E−01	18.8	9.98E−02	33.0
		9662720	767,992,960	3.15	78.1	1.07E−01	17.7	1.20E−01	30.4
HD 089388	20MC	13441024	797,793,856	3.15	52.9	6.04E−01	68.1	6.11E−01	49.0
HD 089484	W	7967232	754,630,208	3.15	78.3	1.08E+00	154.8	1.09E+00	61.0
	21MC	13634560	800,463,488	3.15	78.4	1.01E+00	186.8	1.05E+00	79.7
		13643008	800,736,512	3.15	78.2	1.02E+00	181.9	1.05E+00	75.8
HD 089758	W	7967488	754,630,592	3.15	77.9	1.37E+00	130.6	1.37E+00	70.8
HD 092305	19MC	13308928	794,193,536	3.15	78.0	5.01E−01	120.3	5.03E−01	62.1
	21MC	13590272	800,828,224	3.15	78.1	4.60E−01	125.1	4.69E−01	56.6
HD 093813	22MC	15247872	803,701,696	3.15	77.9	4.57E−01	53.6	4.70E−01	59.2
HD 095689	21MC	13634816	800,476,096	3.15	78.2	1.07E+00	162.4	1.10E+00	91.3
HD 096833	W	7966720	754,628,672	3.15	77.9	3.81E−01	50.2	3.62E−01	40.7
	28MC	16619008	821,403,072	3.15	78.3	3.95E−01	78.3	3.66E−01	44.1
HD 100029	X1	7980032	753,522,304	3.15	78.2	7.76E−01	87.0	7.54E−01	53.6
	20MC	13441280	797,508,096	3.15	53.2	7.75E−01	140.6	7.53E−01	55.8
HD 102647	8MC	9807616	770,512,384	10.49	260.3	4.64E−01	160.7	4.46E−01	58.9
	28MC	16618752	821,404,800	3.15	78.2	5.24E−01	82.8	4.81E−01	53.7
HD 102870	8MC	9807360	770,511,744	10.49	260.3	1.13E−01	42.7	6.79E−02	27.3
HD 108903	18MC	13112832	791,240,640	3.15	53.0	8.79E+00	184.1	1.06E+01	113.3
HD 110304	29MC	16869376	824,530,176	10.49	260.1	6.18E−02	18.7	7.07E−02	25.9
HD 120933	22MC	15248128	804,176,000	3.15	77.9	6.67E−01	151.3	6.79E−01	68.8
HD 121370	29MC	16836608	824,525,248	3.15	77.8	1.55E−01	37.1	1.57E−01	38.6
HD 123123	29MC	16869632	824,529,280	10.49	261.0	2.86E−01	88.9	2.75E−01	43.5
HD 124897	18MC	13113088	791,240,064	3.15	53.1	7.07E+00	181.4	9.16E+00	133.8
HD 131873	W	7967744	754,631,104	3.15	78.3	2.05E+00	164.3	2.09E+00	88.2
	1MC	8343040	755,588,096	3.15	78.2	1.95E+00	213.6	2.03E+00	121.3
	2MC	8381952	757,133,952	3.15	78.4	2.03E+00	207.7	2.12E+00	93.9
		8421376	757,257,280	3.15	78.4	1.92E+00	244.1	2.06E+00	116.1
	16MC	12873728	786,482,624	3.15	78.5	1.94E+00	204.6	2.11E+00	110.8
HD 136422	23MC	15421952	807,195,584	3.15	77.8	6.38E−01	115.3	6.37E−01	63.5
HD 138265	W	7965696	754,626,368	3.15	78.2	7.66E−02	12.4	7.04E−02	25.0
	5MC	9192704	763,724,672	10.49	260.3	7.90E−02	36.1	7.36E−02	36.5
HD 140573	23MC	15422208	807,195,072	3.15	78.3	5.19E−01	146.9	5.23E−01	65.4
HD 141477	24MC	15817984	809,531,968	3.15	78.2	6.81E−01	99.5	6.42E−01	65.9
HD 152222	5MC	9192960	763,699,072	10.49	259.2	2.18E−02	11.3	2.47E−02	19.5
	9MC	9941760	772,169,408	10.49	511.2	3.23E−02	20.9	2.60E−02	29.4
	20MC	13477632	797,099,968	3.15	304.4	2.00E−02	8.3	2.68E−02	21.9
HD 156283	21MC	13590528	801,046,272	3.15	78.3	6.06E−01	149.6	6.09E−01	54.7
HD 159048	17MC	13078272	789,150,272	10.49	510.6	3.05E−02	13.9	1.90E−02	19.1
HD 159330	4MC	9059584	761,921,344	10.49	258.8	3.63E−02	16.1	3.58E−02	22.2
	20MC	13477120	797,222,016	3.15	304.5	4.90E−02	22.2	4.86E−02	38.7
		13477376	797,221,056	10.49	511.3	4.44E−02	30.1	4.11E−02	33.6
	28MC	16619520	821,396,800	10.49	258.7	4.54E−02	18.8	4.14E−02	21.9
HD 163588	R	7606272	753,571,584	3.15	71.4	2.07E−01	57.3	1.99E−01	39.8
		7607040	753,689,280	3.15	78.0	2.10E−01	31.2	1.70E−01	12.0
	V	7795968	754,091,840	3.15	77.9	2.10E−01	48.4	2.08E−01	42.6
	W	7974656	754,603,392	3.15	78.1	2.18E−01	63.9	2.14E−01	49.3
	X1	7980800	753,504,640	3.15	77.8	2.27E−01	31.6	2.12E−01	36.5
		7981056	753,541,632	3.15	78.3	2.06E−01	47.5	1.99E−01	40.8
	1MC	8139008	755,320,896	3.15	78.0	2.16E−01	69.1	2.11E−01	45.2
		8140800	755,397,760	3.15	77.9	2.19E−01	79.0	2.12E−01	45.8
		8141056	755,492,288	3.15	78.1	2.27E−01	68.6	2.18E−01	51.7
		8342272	755,587,008	3.15	78.1	2.09E−01	78.5	2.05E−01	48.2
		8783360	755,756,224	3.15	78.3	2.14E−01	80.6	2.12E−01	50.9
	2MC	8381184	757,132,864	3.15	78.0	2.12E−01	28.3	2.13E−01	41.8
		8383232	757,256,256	3.15	77.9	2.15E−01	57.6	2.06E−01	46.0
	3MC	8809728	759,525,120	3.15	77.8	1.97E−01	55.7	1.92E−01	37.3
		8819456	759,825,024	3.15	77.8	2.12E−01	77.0	1.98E−01	42.2
		8937728	760,265,344	3.15	78.0	2.01E−01	34.5	2.02E−01	31.8
	4MC	9067264	761,709,120	3.15	77.9	2.09E−01	72.2	2.00E−01	42.1

TABLE 2 (*Continued*)

Name	Campaign[a]	AOR Key	Time[b] (s)	Exp. Time (s)	Total Time[c] (s)	Aperture Flux (MIPS70)	S/N	PSF Flux (MIPS70)	S/N
		9067520	762,003,968	3.15	78.1	2.03E−01	52.9	1.83E−01	16.9
		9181696	762,254,336	3.15	78.0	1.72E−01	22.9	1.73E−01	26.6
	5MC	9191168	763,690,560	3.15	78.1	2.06E−01	80.4	1.99E−01	43.1
		9221888	764,024,768	3.15	78.1	2.02E−01	73.9	1.96E−01	41.9
		9222656	764,360,512	3.15	77.9	2.10E−01	70.2	2.00E−01	42.4
	6MC	9617920	766,301,248	3.15	78.0	2.04E−01	70.7	1.98E−01	41.6
	7MC	9658624	767,919,104	3.15	77.7	2.17E−01	90.0	2.09E−01	47.0
		9659136	768,168,000	3.15	77.9	2.08E−01	64.1	2.02E−01	43.1
	8MC	9802752	770,187,072	3.15	78.2	2.10E−01	67.7	2.01E−01	41.7
		9803520	770,600,448	3.15	78.1	2.14E−01	59.7	2.12E−01	45.2
		9804288	770,843,904	3.15	77.9	2.07E−01	62.2	2.02E−01	46.8
	9MC	9937408	772,025,600	3.15	78.1	2.29E−01	76.9	2.17E−01	46.3
		9938944	772,235,776	3.15	77.8	2.21E−01	72.3	2.16E−01	48.3
		9939712	772,483,136	3.15	77.9	2.23E−01	57.4	2.16E−01	39.3
	10MC	10088192	773,705,792	3.15	77.9	2.32E−01	69.7	2.19E−01	46.6
		10088960	773,880,064	3.15	77.9	2.03E−01	59.7	2.03E−01	46.4
		10089728	774,124,928	3.15	77.9	2.32E−01	69.7	2.25E−01	44.5
	11MC	11780608	775,520,128	3.15	78.0	2.16E−01	77.6	2.18E−01	49.8
		11781376	775,821,568	3.15	77.8	2.38E−01	76.4	2.30E−01	48.7
		11782144	776,080,512	3.15	78.2	2.34E−01	90.2	2.23E−01	49.5
		11782912	776,280,384	3.15	77.5	2.39E−01	70.4	2.11E−01	34.5
	12MC	11891456	777,336,320	3.15	78.0	2.23E−01	80.0	2.18E−01	46.4
		11897344	777,592,128	3.15	77.8	2.22E−01	69.5	2.12E−01	45.0
		11898112	778,057,920	3.15	78.0	2.53E−01	74.5	2.26E−01	49.6
	13MC	12060416	779,574,272	3.15	78.1	2.17E−01	67.7	2.16E−01	47.0
		12061184	779,910,912	3.15	78.1	2.33E−01	67.7	2.23E−01	47.7
		12061952	780,221,440	3.15	78.1	2.17E−01	68.6	2.17E−01	49.8
		12153088	780,631,360	3.15	77.8	2.24E−01	65.3	2.14E−01	43.1
	14MC	12194816	782,077,056	3.15	77.9	1.99E−01	61.2	2.04E−01	44.2
		12195584	782,377,792	3.15	78.0	2.14E−01	75.5	2.13E−01	47.9
		12196352	782,680,448	3.15	77.6	2.33E−01	58.4	2.29E−01	50.1
	15MC	12394752	784,175,424	3.15	77.7	2.14E−01	67.1	2.10E−01	46.3
		12395520	783,803,456	3.15	77.9	2.07E−01	56.8	2.04E−01	43.3
		12396288	784,570,880	3.15	78.2	2.36E−01	48.3	2.13E−01	37.2
	18MC	13109504	791,681,152	3.15	77.9	2.22E−01	83.5	2.16E−01	43.5
		13110528	792,003,840	3.15	78.3	2.29E−01	77.2	2.16E−01	46.1
	19MC	13295872	793,828,736	3.15	77.9	2.11E−01	58.2	2.13E−01	43.6
		13298688	794,911,040	3.15	77.9	2.17E−01	60.5	2.13E−01	44.9
		13299712	794,452,928	3.15	78.0	2.11E−01	80.9	2.11E−01	44.8
	20MC	13429248	796,764,160	3.15	77.8	2.22E−01	74.6	2.13E−01	46.1
		13431808	797,812,480	3.15	78.1	2.22E−01	61.2	2.11E−01	41.9
		13432576	797,325,952	3.15	77.9	2.17E−01	70.4	2.10E−01	45.5
	21MC	13585664	801,062,848	3.15	77.8	2.14E−01	67.6	2.11E−01	43.4
		13586432	800,229,760	3.15	77.7	2.07E−01	77.9	2.06E−01	44.6
		13587968	801,073,984	3.15	78.2	2.23E−01	62.2	2.18E−01	46.1
	22MC	15217408	803,340,736	3.15	77.7	2.23E−01	93.3	2.15E−01	44.5
		15220736	803,958,208	3.15	77.6	2.22E−01	58.3	2.18E−01	41.5
		15221760	804,509,888	3.15	78.3	2.22E−01	68.3	2.19E−01	47.3
	23MC	15413504	806,870,208	3.15	78.1	2.28E−01	65.2	2.18E−01	45.9
		15414528	807,165,184	3.15	78.3	2.38E−01	60.5	2.12E−01	43.3
		15415552	807,541,888	3.15	77.9	2.27E−01	57.5	2.01E−01	30.6
	24MC	15815424	809,473,536	3.15	78.2	2.24E−01	65.4	2.10E−01	42.5
		15816448	809,843,584	3.15	78.1	2.21E−01	67.3	2.18E−01	45.0
		15817472	810,383,680	3.15	78.2	2.24E−01	57.1	2.05E−01	44.6
	25MC	15991296	811,962,816	3.15	78.1	2.16E−01	69.9	2.09E−01	46.2
		16047872	812,608,960	3.15	77.5	2.21E−01	60.2	2.15E−01	45.7
		16048896	813,301,568	3.15	78.0	2.10E−01	72.6	2.04E−01	43.3
	26MC	16228864	815,420,352	3.15	77.8	2.15E−01	60.3	2.12E−01	41.8
		16254464	815,882,816	3.15	77.9	2.05E−01	58.3	2.07E−01	43.7
		16255488	816,317,440	3.15	78.0	2.16E−01	57.9	2.13E−01	43.7
	27MC	16374784	817,788,288	3.15	77.5	2.02E−01	50.5	1.99E−01	40.3
		16375552	818,043,200	3.15	78.1	2.21E−01	56.7	2.16E−01	45.0

TABLE 2 (*Continued*)

Name	Campaign[a]	AOR Key	Time[b] (s)	Exp. Time (s)	Total Time[c] (s)	Aperture Flux (MIPS70)	S/N	PSF Flux (MIPS70)	S/N
	29MC	16834048	824,364,800	3.15	77.9	2.27E−01	68.5	2.13E−01	43.8
		16835072	824,955,200	3.15	78.2	2.25E−01	78.2	2.13E−01	44.1
		16836096	825,856,512	3.15	77.8	2.12E−01	68.2	2.07E−01	43.5
HD 164058	20MC	13441536	797,285,056	3.15	53.2	1.87E+00	224.3	2.11E+00	101.0
HD 166780	19MC	13314816	793,927,168	10.49	511.0	1.96E−02	7.6	1.80E−02	19.2
HD 169916	6MC	9458688	766,047,296	10.49	259.6	3.52E−01	27.7	2.90E−01	34.8
		9458944	766,047,872	3.15	78.1	3.45E−01	25.1	2.92E−01	32.5
HD 170693	W	7965184	754,625,024	3.15	77.7	8.73E−02	13.0	8.84E−02	24.7
	29MC	16869888	824,523,456	10.49	258.7	9.39E−02	18.3	9.31E−02	39.2
HD 173398	18MC	13112576	791,238,784	10.49	510.1	4.75E−02	31.9	4.32E−02	32.6
	29MC	16870144	824,524,224	10.49	259.5	3.69E−02	19.2	4.31E−02	23.5
HD 173511	17MC	12998400	789,152,320	10.49	510.1	1.50E−02	6.4	1.35E−02	12.3
HD 173976	6MC	9459456	766,034,816	10.49	260.1	2.44E−02	14.2	2.36E−02	19.6
	9MC	9942016	772,171,456	10.49	509.7	2.10E−02	10.1	2.16E−02	23.0
	17MC	12998144	789,151,360	10.49	511.3	2.10E−02	13.6	2.12E−02	24.0
	20MC	13478144	797,808,000	3.15	304.4	1.93E−02	8.3	2.20E−02	21.7
		13478400	797,808,704	10.49	511.0	1.79E−02	9.8	2.23E−02	22.8
HD 180711	W	7966208	754,627,584	3.15	77.9	2.95E−01	45.7	2.79E−01	43.4
	4MC	9068032	761,710,080	3.15	78.1	2.69E−01	68.3	2.61E−01	39.5
		9068288	762,004,928	3.15	78.0	2.70E−01	70.5	2.52E−01	30.8
		9181952	762,260,928	3.15	77.7	2.35E−01	29.3	2.39E−01	28.1
	5MC	9191424	763,691,456	3.15	78.2	2.84E−01	84.1	2.73E−01	49.5
		9222144	764,025,664	3.15	78.1	2.76E−01	98.5	2.48E−01	24.4
	8MC	9803008	770,188,032	3.15	78.4	2.68E−01	68.6	2.63E−01	46.9
		9803776	770,601,344	3.15	78.0	2.69E−01	80.1	2.67E−01	49.7
		9804544	770,844,800	3.15	78.2	2.59E−01	85.1	2.52E−01	43.6
	9MC	9937664	772,026,496	3.15	78.4	2.98E−01	95.9	2.82E−01	53.1
		9939200	772,236,672	3.15	77.7	2.72E−01	76.1	2.73E−01	48.3
		9939968	772,484,032	3.15	78.1	3.01E−01	71.7	2.90E−01	50.6
	10MC	10088448	773,706,752	3.15	77.8	2.89E−01	72.1	2.77E−01	45.2
		10089216	773,881,024	3.15	77.9	2.78E−01	85.2	2.74E−01	49.5
		10089984	774,125,888	3.15	78.1	3.03E−01	89.8	2.90E−01	49.5
	11MC	11780864	775,521,024	3.15	78.1	2.89E−01	82.2	2.80E−01	50.4
		11781632	775,822,464	3.15	78.0	2.95E−01	80.8	2.76E−01	51.5
		11782400	776,081,472	3.15	77.8	3.02E−01	84.1	2.90E−01	50.4
		11783168	776,281,344	3.15	78.3	2.80E−01	82.7	2.82E−01	51.5
	12MC	11891712	777,337,280	3.15	78.0	2.90E−01	84.9	2.70E−01	48.5
		11897600	777,593,088	3.15	77.7	2.80E−01	77.5	2.79E−01	45.6
		11898368	778,058,816	3.15	77.9	2.83E−01	63.4	2.76E−01	45.2
	13MC	12060672	779,575,168	3.15	78.1	3.13E−01	86.8	2.74E−01	38.6
		12061440	779,911,808	3.15	78.3	2.99E−01	90.1	2.91E−01	51.0
		12062208	780,222,336	3.15	78.3	3.02E−01	104.3	2.98E−01	53.2
		12153344	780,632,320	3.15	77.8	2.95E−01	82.4	2.86E−01	48.9
	14MC	12195072	782,077,952	3.15	77.9	2.78E−01	83.5	2.70E−01	49.0
		12195840	782,378,752	3.15	77.7	2.80E−01	79.2	2.79E−01	51.4
		12196608	782,681,408	3.15	78.3	3.09E−01	86.2	3.07E−01	60.3
	15MC	12395008	784,176,384	3.15	78.3	2.85E−01	77.2	2.83E−01	52.8
		12395776	783,804,352	3.15	78.0	2.76E−01	71.6	2.69E−01	47.5
		12396544	784,571,840	3.15	78.1	2.96E−01	61.9	2.85E−01	46.5
	16MC	12871680	786,141,952	3.15	78.0	2.90E−01	85.8	2.81E−01	49.0
		12884480	786,574,272	3.15	78.4	3.03E−01	90.2	2.94E−01	50.5
		12884992	786,900,864	3.15	77.9	2.81E−01	74.9	2.72E−01	47.0
	17MC	12997376	788,129,216	3.15	78.0	2.92E−01	107.2	2.82E−01	52.6
		13001728	788,494,656	3.15	78.1	2.77E−01	67.9	2.78E−01	48.0
		13072896	789,156,032	3.15	77.9	2.99E−01	82.4	2.83E−01	45.2
	18MC	13109248	790,894,272	3.15	78.2	2.75E−01	65.2	2.71E−01	46.3
		13110272	792,002,816	3.15	77.9	2.77E−01	91.4	2.70E−01	47.4
		13111296	791,342,528	3.15	77.8	2.80E−01	89.0	2.74E−01	48.8
	19MC	13295616	793,827,456	3.15	77.9	2.88E−01	99.6	2.66E−01	48.5
		13298432	794,454,208	3.15	78.3	2.86E−01	92.2	2.81E−01	51.6
		13299456	794,910,016	3.15	78.3	2.82E−01	99.2	2.78E−01	53.1
	22MC	15217664	803,341,952	3.15	77.9	2.94E−01	77.2	2.78E−01	48.3

TABLE 2 (*Continued*)

Name	Campaign[a]	AOR Key	Time[b] (s)	Exp. Time (s)	Total Time[c] (s)	Aperture Flux (MIPS70)	S/N	PSF Flux (MIPS70)	S/N
		15220992	803,956,992	3.15	77.8	2.87E−01	86.7	2.82E−01	47.4
		15222016	804,511,168	3.15	78.0	2.91E−01	76.4	2.86E−01	51.7
	23MC	15413760	806,871,168	3.15	77.2	2.75E−01	71.4	2.71E−01	46.3
		15414784	807,166,400	3.15	78.3	2.72E−01	86.6	2.66E−01	46.3
		15415808	807,540,672	3.15	78.0	2.76E−01	70.5	2.77E−01	50.4
	24MC	15815680	809,474,496	3.15	78.2	2.81E−01	81.6	2.75E−01	49.1
		15816704	809,844,544	3.15	78.3	2.85E−01	84.5	2.82E−01	49.7
		15817728	810,384,640	3.15	77.9	2.72E−01	81.0	2.71E−01	45.8
	25MC	15991552	811,963,136	3.15	78.0	2.85E−01	83.1	2.69E−01	45.0
		16048128	812,608,576	3.15	78.1	2.88E−01	83.2	2.79E−01	49.4
		16049152	813,301,952	3.15	77.6	2.75E−01	82.0	2.55E−01	47.0
	26MC	16229120	815,420,672	3.15	78.0	2.91E−01	90.5	2.76E−01	48.6
		16254720	815,883,392	3.15	77.7	2.99E−01	78.0	2.72E−01	48.7
		16255744	816,317,824	3.15	77.5	2.73E−01	75.4	2.70E−01	48.8
	27MC	16375040	817,789,248	3.15	77.6	2.86E−01	60.7	2.78E−01	43.6
		16375808	818,044,224	3.15	77.9	2.88E−01	92.1	2.82E−01	48.4
		16377344	818,481,664	3.15	77.8	3.07E−01	74.5	2.76E−01	47.6
	28MC	16603136	820,974,720	3.15	78.0	2.80E−01	85.3	2.67E−01	46.9
		16603904	821,395,200	3.15	78.0	2.93E−01	90.5	2.72E−01	48.4
		16604672	821,607,616	3.15	77.8	2.87E−01	96.1	2.77E−01	48.0
	29MC	16834304	824,363,584	3.15	77.8	2.94E−01	85.6	2.81E−01	46.3
		16835328	824,956,160	3.15	77.9	2.86E−01	91.6	2.74E−01	47.0
		16836352	825,855,040	3.15	77.8	2.82E−01	92.7	2.72E−01	48.4
HD 183439	7MC	9662208	767,993,792	3.15	78.1	3.32E−01	77.4	3.43E−01	46.3
HD 197989	21MC	13590784	801,047,296	3.15	78.0	5.02E−01	105.7	4.95E−01	52.7
HD 198542	21MC	13591040	801,047,872	3.15	78.2	5.25E−01	114.7	5.06E−01	55.2
HD 209952	R	7602176	753,650,688	10.49	259.3	8.28E−02	22.5	7.11E−02	29.8
	X1	7979008	753,516,608	3.15	77.5	9.69E−02	13.4	7.77E−02	20.4
	7MC	9661696	768,552,960	10.49	259.1	7.19E−02	30.9	7.39E−02	34.7
	21MC	13642240	800,777,728	3.15	153.4	7.70E−02	32.1	6.89E−02	39.0
HD 213310	W	7966976	754,629,376	3.15	78.1	6.72E−01	79.6	6.74E−01	54.6
	22MC	15248384	804,442,624	3.15	78.2	6.60E−01	155.1	6.78E−01	62.0
HD 216131	W	7965952	754,627,008	3.15	77.6	2.30E−01	42.2	2.21E−01	40.6
HD 217906	11MC	11784192	775,641,728	3.15	78.4	4.55E+00	235.2	5.68E+00	135.9

[a] The letter (for in-orbit checkout) or number of the MIPS campaign (MC) in which the observations were taken.

[b] The time the exposure started is the number of seconds from 1980 January 1.

[c] The total exposure time is computed as the average exposure time per pixel in the object aperture to account for exposure time lost to cosmic-ray rejection.

3. RESULTS

The first step in deriving the final calibration factor is to examine the ensemble of calibration factor measurements for stars that show significant deviations. These deviations can be the result of a star having an infrared excess, a poor flux density prediction, or a measurement corrupted by extended emission. Infrared excesses and poor flux density predictions can be seen by calculating the calibration factor for each star and identifying stars that give calibration factors that are significantly deviant from the ensemble. Stars with excesses will have measured flux densities well in excess of the predicted flux densities and, thus, will predict low calibration factors compared to nonexcess stars. Figure 3 displays the calibration factors for all the calibration stars versus predicted flux density. The calibration factors are calculated as a conversion from MIPS70 units to MJy sr^{-1}, as the basic measurement made by the 70 μm detectors is flux per pixel, which is a surface brightness (see § 3.6 for the conversion from MIPS70 units directly to flux densities assuming the default 70 μm mosaic pixel size). Measurements using both aperture photometry and PSF fitting are shown in this figure. The PSF fitting values show less scatter than the aperture photometry values and, thus, will be the basis for identifying deviant measurements. We identify two stars (HD 102647 and HD 173398) that have possible excesses from Figure 3 and no stars with poor flux density predictions. There are seven stars that have significant extended emission underlying or near the object position determined by visual inspection of the 70 μm images. During this inspection, it was seen that the observation of HD 173511 was affected by a nearby, much brighter object, and, as a result, this star was also rejected. The stars in our sample that have been rejected for any of these three reasons are listed in Table 6. If a star was rejected as part

TABLE 3
FINE-SCALE MEASUREMENTS

Name	Campaign[a]	AOR Key	Time[b] (s)	Exp. Time (s)	Total Time[c] (s)	Aperture Flux (MIPS70F)	S/N	PSF Flux (MIPS70F)	S/N
HD 045348	6MC	9456384	765,978,944	10.49	187.1	1.66E+00	139.0	1.56E+00	111.0
HD 048915	6MC	9456896	765,977,024	10.49	186.3	1.52E+00	119.2	1.47E+00	118.2
HD 071129	29MC	16863744	825,634,368	10.49	124.3	2.90E+00	208.3	2.68E+00	102.0
HD 080493	21MC	13635072	800,352,640	10.49	248.7	9.89E−01	148.9	9.03E−01	125.0
HD 082668	7MC	9653248	768,348,480	10.49	248.4	9.53E−01	67.9	8.75E−01	126.5
HD 100029	5MC	9189888	763,723,136	10.49	186.7	6.47E−01	104.2	6.20E−01	100.8
HD 108903	18MC	13113600	791,361,728	10.49	251.2	1.09E+01	282.4	9.83E+00	163.8
HD 131873	1MC	8343296	755,588,352	3.15	56.0	1.80E+00	106.0	1.76E+00	110.6
	2MC	8382208	757,134,208	3.15	55.7	1.76E+00	88.0	1.63E+00	100.7
		8422400	757,257,536	3.15	55.7	1.81E+00	92.2	1.71E+00	100.0
	5MC	9190400	763,697,536	10.49	186.9	1.76E+00	201.6	1.62E+00	93.8
HD 163588	R	7606528	753,571,776	3.15	55.8	2.29E−01	15.7	1.78E−01	31.7
		7607296	753,689,536	3.15	55.7	1.71E−01	10.1	1.67E−01	32.8
	V	7796224	754,091,456	3.15	55.3	2.21E−01	12.2	1.94E−01	34.7
	W	7974912	754,603,648	3.15	55.6	2.20E−01	13.7	2.00E−01	32.9
	1MC	8141568	755,321,152	3.15	55.5	2.25E−01	16.3	1.81E−01	38.2
		8141824	755,398,016	3.15	55.7	1.66E−01	9.7	1.99E−01	34.1
		8142080	755,492,480	3.15	55.4	2.01E−01	14.8	1.94E−01	35.3
		8342528	755,587,264	3.15	55.6	2.44E−01	15.3	1.96E−01	35.6
		8783616	755,756,480	3.15	55.6	1.67E−01	12.5	1.87E−01	45.0
	2MC	8381440	757,133,120	3.15	55.7	1.85E−01	9.0	1.65E−01	28.7
		8384256	757,256,448	3.15	55.6	2.43E−01	15.2	1.84E−01	37.1
	26MC	16276736	815,937,216	10.49	562.2	1.99E−01	43.0	1.77E−01	70.3
HD 217906	16MC	12868608	786,224,896	10.49	249.9	5.14E+00	369.8	4.70E+00	136.8

[a] The letter (for in-orbit checkout) or number of the MIPS campaign (MC) in which the observations were taken.
[b] The time the exposure started is the number of seconds from 1980 January 1.
[c] The total exposure time is computed as the average exposure time per pixel in the object aperture to account for exposure time lost to cosmic-ray rejection.

of the 24 μm analysis given in Engelbracht et al. (2007), it is not used at all in this paper.

3.1. Flux Density/Background Nonlinearities

A possible source of scatter in the calibration factor measurements is flux density nonlinearities that are a characteristic of Ge:Ga detectors. In contrast to electronic nonlinearities that depend solely on total flux density, flux density nonlinearities are due to the change in rate of flux density falling on the detectors (e.g., when a source chops onto a detector). Given that the nonlinearity is due to a change in flux density on the detector, the flux density nonlinearity could depend on background as well as source flux density. The electronic nonlinearities are small (~2%) for the MIPS 70 μm pixels and are corrected when the data are reduced (Gordon et al. 2005). Figure 4 shows the calibration factors versus predicted flux densities and backgrounds. The calibration factors have been calculated from the average of all the measurements of each star, and the uncertainty on the average includes the flux density prediction uncertainty. The calculated calibration factors for each star are listed in Tables 4 and 5.

It is clear that flux density nonlinearities are present in the aperture photometry data but are much smaller or nonexistent in the PSF fitting photometry. A direct comparison of the aperture

and PSF fitting measurements is shown in Figure 5. Starting at around ~1 Jy, the aperture measurements begin to underestimate the PSF measurements, while below ~200 mJy, the aperture–to–PSF fitting ratio shows a large scatter. For bright sources, the flux density nonlinearities will show up at the peak of the PSF and the PSF fitting compensates as relatively more weight is given to the wings of the PSF than in aperture photometry. For faint sources, the PSF fitting shows less scatter, since it more accurately accounts for nearby faint sources and background structure than aperture photometry. For these reasons, we use the PSF fitting measurements for the rest of this work.

The PSF fitting measurements show that the 70 μm calibration measurements are linear between 22 mJy and 17 Jy. A linear fit to these data (accounting for the uncertainties in both x- and y-values) gives

$$\text{Factor} = (691 \pm 18) + (4.0 \pm 5.9) \log [F(\nu)], \quad (1)$$

where $F(\nu)$ is the flux density in mJy. There are five stars (HD 31398, 120933, 213310, 216131, and 217906) that are >5 σ from the mean calibration factor and are identified with square boxes in Figure 4. The large deviations of these five stars are most likely due to weak infrared excesses, as the derived calibration factor is low compared to the ensemble.

TABLE 4
COARSE-SCALE CALIBRATION FACTORS

NAME	SPECTRAL TYPE	PREDICTED (mJy)		BACK-GROUND (MJy sr⁻¹)		AVERAGE MEASURED[a] (MIPS70)				CALIBRATION FACTOR (MJy sr⁻¹ MIPS70⁻¹)			
		Flux	Unc.	SB	Unc	Ap. Flux	S/N	PSF Flux	S/N	Ap.	Unc.	PSF	Unc.
HD 002151	G2 IV	255.6	8.9	5.3	0.6	1.53E−01	54.2	1.59E−01	68.8	734.8	29.0	706.0	26.7
HD 002261	K0 III	1138.0	59.6	6.3	0.5	7.15E−01	49.7	6.88E−01	58.3	697.5	39.2	725.5	40.0
HD 003712	K0 IIIa	1180.0	47.6	10.9	0.8	7.11E−01	55.5	7.37E−01	70.2	727.9	32.2	702.3	30.1
HD 004128	K0 III	1205.0	40.1	10.1	1.1	6.98E−01	52.7	6.90E−01	63.6	757.5	29.0	765.7	28.2
HD 006860	M0 III	5334.0	202.2	8.5	1.3	3.04E+00	70.9	3.40E+00	96.6	768.4	31.1	687.9	27.0
HD 009053	M0 IIIa	1504.0	64.9	5.7	0.3	8.85E−01	62.2	9.10E−01	78.0	744.9	34.3	724.5	32.6
HD 009927	K3 III	472.2	15.8	8.9	1.0	2.95E−01	57.7	2.84E−01	67.8	701.6	26.4	728.4	26.6
HD 012533	K3 IIb	1985.0	67.2	8.8	1.3	1.24E+00	63.8	1.30E+00	81.5	699.5	26.1	667.9	24.1
HD 012929	K2 III	1734.0	57.8	13.7	2.7	1.04E+00	56.0	1.08E+00	70.7	731.5	27.7	706.1	25.6
HD 015008	A1/2 V	22.0	0.8	4.7	0.6	1.79E−02	26.3	1.25E−02	22.4	539.0	28.3	770.0	44.1
HD 018884	M1.5 III	4645.0	160.1	14.4	2.2	2.60E+00	79.0	2.89E+00	107.4	784.6	28.8	704.4	25.1
HD 020902	F5 I	510.7	19.2	15.2	1.4	3.13E−01	26.3	3.02E−01	30.9	714.5	38.2	741.9	36.8
HD 024512	M2 III	2421.0	94.0	6.1	0.6	1.41E+00	102.1	1.47E+00	130.3	754.7	30.2	721.2	28.6
HD 025025	M1 IIIb	2320.0	82.5	8.0	0.8	1.48E+00	67.3	1.55E+00	86.1	687.5	26.5	655.5	24.5
HD 029139	K5 III	12840.0	451.2	23.7	3.1	5.96E+00	71.2	7.87E+00	114.8	944.8	35.8	715.1	25.9
HD 031398[b]	K3 II	1560.0	65.8	26.6	2.9	1.11E+00	60.4	1.20E+00	79.3	615.5	27.9	572.1	25.2
HD 032887	K4 III	1159.0	40.5	6.1	0.8	7.31E−01	50.7	7.25E−01	61.3	695.0	27.9	700.9	27.0
HD 034029	G5 IIIe+	5095.0	201.8	19.4	1.8	2.72E+00	126.4	2.99E+00	169.4	821.0	33.2	747.8	29.9
HD 035666[b]	K3 III	26.9	1.1	6.2	0.5	1.77E−02	19.5	1.76E−02	23.5	665.3	43.1	671.7	39.0
HD 036167[b]	K5 III	417.1	26.5	17.5	1.6	2.56E−01	45.9	2.36E−01	51.7	714.5	47.9	774.1	51.3
HD 039425	K2 III	587.7	19.2	5.2	0.7	3.52E−01	14.7	2.89E−01	14.7	732.5	55.4	892.8	67.4
HD 039608	K5 III	29.7	1.2	5.0	0.5	2.66E−02	32.7	2.14E−02	32.0	488.2	24.7	608.5	31.0
HD 042701[b]	K3 III	33.8	1.0	5.1	0.6	6.10E−02	54.8	3.18E−02	34.8	242.7	8.1	465.5	18.7
HD 045348	F0 II	3085.0	67.1	5.6	0.5	1.75E+00	89.5	1.84E+00	114.9	772.2	18.9	733.5	17.2
HD 048915	A0 V	2900.0	354.5	14.8	1.0	1.60E+00	79.1	1.68E+00	101.1	793.3	97.5	757.5	92.9
HD 050310	K1 III	706.0	24.7	5.8	0.6	4.37E−01	67.4	4.26E−01	80.2	708.0	26.9	725.9	27.0
HD 051799	M1 III	593.1	20.0	5.4	0.6	3.98E−01	57.8	3.84E−01	68.2	654.2	24.8	676.7	24.9
HD 053501	K3 III	143.3	4.5	6.0	0.6	9.95E−02	43.6	8.30E−02	44.4	631.8	24.5	757.3	29.1
HD 056855	K3 Ib	2544.0	81.3	8.7	0.7	1.61E+00	63.5	1.77E+00	85.3	694.3	24.7	629.8	21.4
HD 059717	K5 III	1423.0	49.0	8.2	0.6	8.89E−01	60.7	9.23E−01	76.9	702.3	26.8	675.9	24.9
HD 060522	M0 III	746.5	25.5	15.2	3.2	4.54E−01	34.4	4.56E−01	42.1	720.5	32.3	718.0	29.8
HD 062509	K0 IIIb	2607.0	79.1	14.7	3.1	1.56E+00	73.2	1.64E+00	93.7	732.1	24.4	697.0	22.4
HD 071129	K3 III+	5153.0	168.7	7.5	0.6	2.85E+00	160.5	3.17E+00	217.8	792.9	26.4	713.1	23.6
HD 080007	A2 IV	199.9	6.1	5.6	0.6	1.38E−01	47.1	1.26E−01	52.5	635.0	23.5	695.1	24.9
HD 080493	K7 III	1686.0	60.0	10.8	1.9	1.02E+00	86.4	1.07E+00	110.0	721.6	27.0	691.1	25.4
HD 081797	K3 II–III	2887.0	101.1	9.2	1.7	1.76E+00	74.3	1.86E+00	95.9	720.1	27.0	680.8	24.9
HD 082308	K5 III	542.7	20.3	14.5	2.9	3.28E−01	44.3	3.21E−01	52.8	725.3	31.6	742.2	31.1
HD 082668	K5 III	1424.0	204.5	25.7	0.5	9.36E−01	69.9	9.29E−01	84.6	667.1	96.3	672.4	96.9
HD 087901	B7	196.0	5.6	15.3	3.3	1.04E−01	41.6	1.08E−01	52.8	824.3	30.7	793.0	27.1
HD 089388	K3 IIa	820.1	187.9	14.1	0.6	6.04E−01	39.8	6.11E−01	49.0	595.4	137.2	589.0	135.5
HD 089484	K1 IIIb	1744.0	52.1	14.1	2.7	1.03E+00	100.3	1.06E+00	125.8	741.7	23.4	721.4	22.3
HD 089758	M0 III	2192.0	78.5	8.1	1.1	1.37E+00	57.8	1.37E+00	70.8	702.8	28.0	699.4	26.9
HD 092305	M0 III	746.3	29.8	9.6	0.6	4.81E−01	68.0	4.87E−01	83.9	680.2	28.9	672.4	28.0
HD 093813	K0/K1 III	699.0	23.7	9.3	1.5	4.57E−01	47.1	4.70E−01	59.2	671.4	26.9	652.4	24.7
HD 095689	K0 Iab	1694.0	53.2	5.4	0.6	1.07E+00	72.7	1.10E+00	91.3	694.4	23.8	674.5	22.4
HD 096833	K1 III	626.2	20.1	7.0	0.7	3.89E−01	52.5	3.64E−01	60.0	706.2	26.3	753.7	27.2
HD 100029	M0 III	1124.0	38.2	4.9	0.6	7.76E−01	65.3	7.53E−01	77.4	635.5	23.7	654.2	23.8
HD 102647[b]	A3 V	141.4	4.5	13.2	2.0	4.89E−01	69.2	4.61E−01	79.6	126.8	4.4	134.5	4.6
HD 102870	F9 V	108.1	7.3	15.2	3.3	1.13E−01	37.3	6.79E−02	27.3	418.0	30.2	698.1	53.4
HD 108903	M3.5 III	17000.0	1766.0	18.4	0.8	8.79E+00	77.2	1.06E+01	113.3	848.4	88.8	705.5	73.6
HD 110304	A1 IV	119.8	3.2	7.8	0.8	6.18E−02	18.6	7.07E−02	25.9	850.7	51.1	742.8	34.8
HD 120933[b]	K5 III	834.4	30.6	6.2	0.2	6.67E−01	55.4	6.79E−01	68.8	548.5	22.4	539.0	21.3
HD 121370	G 0IV	260.9	10.2	8.3	0.7	1.55E−01	31.2	1.57E−01	38.6	740.1	37.5	730.5	34.3
HD 123123	K2 III	490.9	16.4	12.2	2.2	2.86E−01	37.1	2.75E−01	43.5	751.8	32.2	782.6	31.7
HD 124897	K1.5 III	14340.0	778.8	7.9	0.6	7.07E+00	84.6	9.16E+00	133.8	889.9	49.5	686.3	37.6
HD 131873	K4 III	3363.0	123.7	4.4	0.5	1.97E+00	185.6	2.07E+00	238.9	749.6	27.9	710.7	26.3
HD 136422	K5 III	1042.0	41.0	13.6	2.1	6.38E−01	52.2	6.37E−01	63.5	715.8	31.3	717.4	30.4
HD 138265	K5 III	111.4	3.8	4.4	0.4	7.82E−02	39.1	7.25E−02	44.2	625.0	26.6	673.8	27.5
HD 140573	K2 IIIb	883.8	28.3	9.1	1.2	5.19E−01	53.2	5.23E−01	65.4	746.9	27.7	740.5	26.3

TABLE 4 (*Continued*)

Name	Spectral Type	Predicted (mJy) Flux	Unc.	Background (MJy sr⁻¹) SB	Unc	Average Measured[a] (MIPS70) Ap. Flux	S/N	PSF Flux	S/N	Calibration Factor (MJy sr⁻¹ MIPS70⁻¹) Ap.	Unc.	PSF	Unc.
HD 141477[b]	M0.5 III	921.5	32.4	7.1	0.7	6.81E−01	57.3	6.42E−01	65.9	593.5	23.3	629.5	24.1
HD 152222	K2 III	37.9	1.8	4.5	0.5	2.65E−02	34.8	2.59E−02	41.5	626.7	34.2	641.8	33.6
HD 156283	K3 Iab	940.4	30.8	5.1	0.6	6.06E−01	44.6	6.09E−01	54.7	680.9	27.0	677.2	25.4
HD 159048	K0 III	26.9	0.9	4.7	0.5	3.05E−02	25.1	1.90E−02	19.1	387.0	19.9	622.5	38.4
HD 159330	K2 III	61.7	2.0	4.6	0.4	4.44E−02	51.1	4.25E−02	59.7	608.4	22.8	635.6	23.0
HD 163588	K2 III	354.4	9.9	4.7	0.4	2.18E−01	335.0	2.11E−01	395.7	714.3	20.1	737.9	20.7
HD 164058	K5 III	3315.0	99.7	4.9	0.5	1.87E+00	73.6	2.11E+00	101.0	775.7	25.6	690.2	21.8
HD 166780[b]	K4.5 III	23.8	1.0	4.9	0.4	1.96E−02	17.1	1.80E−02	19.2	532.7	37.9	580.9	38.4
HD 169916[b]	K1 IIIb	675.8	27.5	22.3	3.3	3.49E−01	46.8	2.91E−01	47.6	849.5	39.1	1019.2	46.7
HD 170693	K1.5 III	147.7	4.4	4.8	0.5	9.19E−02	38.1	9.16E−02	46.4	705.0	28.0	706.7	25.9
HD 173398	K0 III	23.9	0.9	4.8	0.5	4.39E−02	33.4	4.32E−02	40.1	238.6	11.6	242.3	11.1
HD 173511[b]	K5 III	24.5	0.9	4.8	0.5	1.50E−02	11.2	1.35E−02	12.3	713.9	68.3	792.5	70.0
HD 173976[b]	K5 III	35.8	1.2	4.6	0.5	2.05E−02	37.9	2.20E−02	49.7	765.6	32.9	712.6	28.1
HD 180711	G9 III	447.4	11.9	4.8	0.6	2.86E−01	333.7	2.76E−01	393.8	686.6	18.3	709.8	18.9
HD 183439	M0 III	575.2	24.9	20.6	0.9	3.32E−01	36.7	3.43E−01	46.3	760.4	38.9	735.2	35.5
HD 197989	K0 III	850.9	34.3	11.2	0.8	5.02E−01	43.8	4.95E−01	52.7	743.2	34.5	753.1	33.6
HD 198542	M0 III	828.5	35.7	15.0	3.1	5.25E−01	46.9	5.06E−01	55.2	692.1	33.3	718.0	33.6
HD 209952	B7 IV	112.7	3.8	7.5	1.1	7.86E−02	57.1	7.16E−02	63.4	628.4	24.0	690.6	25.9
HD 213310[b]	M0 II+	773.3	33.9	7.5	0.5	6.66E−01	66.6	6.76E−01	82.6	509.5	23.6	501.4	22.8
HD 216131[b]	G8 II	249.9	8.4	8.9	1.0	2.30E−01	34.6	2.21E−01	40.6	476.3	21.1	495.2	20.7
HD 217906[b]	M2.5 II	7348.0	273.6	8.2	0.9	4.55E+00	89.3	5.68E+00	135.9	707.5	27.5	567.1	21.5

[a] The measured instrumental flux densities can be converted to physical units by multiplying by 1.60 Jy MIPS70⁻¹.

[b] Stars not used for the final calibration factor, as they were rejected as known outliers (§ 3) or clipped as being >5 σ from the mean (§ 3.1).

These five stars have been excluded from the fit and from the rest of the paper. The slope value is consistent with no nonlinearities; the upper limit on the nonlinearities is computed to be 1.5% from the ratio of the fit values at 10 mJy and 20 Jy. The fit to the aperture photometry shows a 42% nonlinearity between the same limits.

A similar result is found for the calibration factor versus background. The linear fit to the PSF fitting results gives a slope of 54 ± 18, which is consistent with no slope at the 3 σ level. There is a statistically significant slope for the linear fit for the aperture photometry results, but this may just be an artifact of the nonlinearity seen versus flux density. A comparison of the two left-hand plots in Figure 4 shows that the correlation is better versus flux density than versus background.

3.2. Repeatability

The photometric repeatability and trends in time can be measured from the two stars that have been observed throughout MIPS operations. The photometric repeatability is how well the raw flux of a star can be measured and is determined from multiple observations of the same star. Each measured flux

TABLE 5
Fine-Scale Calibration Factors

Name	Spectral Type	Predicted (mJy) Flux	Unc.	Background (MJy sr⁻¹) SB	Unc	Average Measured[a] (MIPS70) Ap. Flux	S/N	PSF Flux	S/N	Calibration Factor (MJy sr⁻¹ MIPS70⁻¹) Ap.	Unc.	PSF	Unc.
HD 045348	F0 II	3085.0	67.1	5.6	0.5	1.66E+00	97.6	1.56E+00	111.0	2881.5	69.3	3066.1	72.2
HD 048915	A0 V	2900.0	354.5	14.8	1.0	1.52E+00	100.6	1.47E+00	118.2	2959.1	362.9	3048.6	373.6
HD 071129	K3 III+	5153.0	168.7	7.5	0.6	2.90E+00	91.3	2.68E+00	102.0	2752.9	95.0	2980.0	101.8
HD 080493	K7 III	1686.0	60.0	10.8	1.9	9.89E−01	113.1	9.03E−01	125.0	2642.6	96.9	2892.3	105.5
HD 082668	K5 III	1424.0	204.5	25.7	0.5	9.53E−01	113.8	8.75E−01	126.5	2316.5	333.3	2522.1	362.8
HD 100029	M0 III	1124.0	38.2	4.9	0.6	6.47E−01	87.0	6.20E−01	100.8	2691.4	96.7	2809.9	99.6
HD 108903	M3.5 III	17000.0	1766.0	18.4	0.8	1.09E+01	150.5	9.83E+00	163.8	2410.5	250.9	2679.5	278.8
HD 131873	K4 III	3363.0	123.7	4.4	0.5	1.78E+00	177.5	1.68E+00	202.8	2925.0	108.8	3098.2	115.0
HD 163588	K2 III	354.4	9.9	4.7	0.4	2.03E−01	125.3	1.83E−01	136.4	2700.1	78.5	3002.0	86.7
HD 217906	M2.5 II	7348.0	273.6	8.2	0.9	5.14E+00	123.5	4.70E+00	136.8	2215.1	84.4	2420.0	91.8

[a] The measured instrumental flux densities can be converted to physical units by multiplying by 1.87 Jy MIPS70⁻¹.

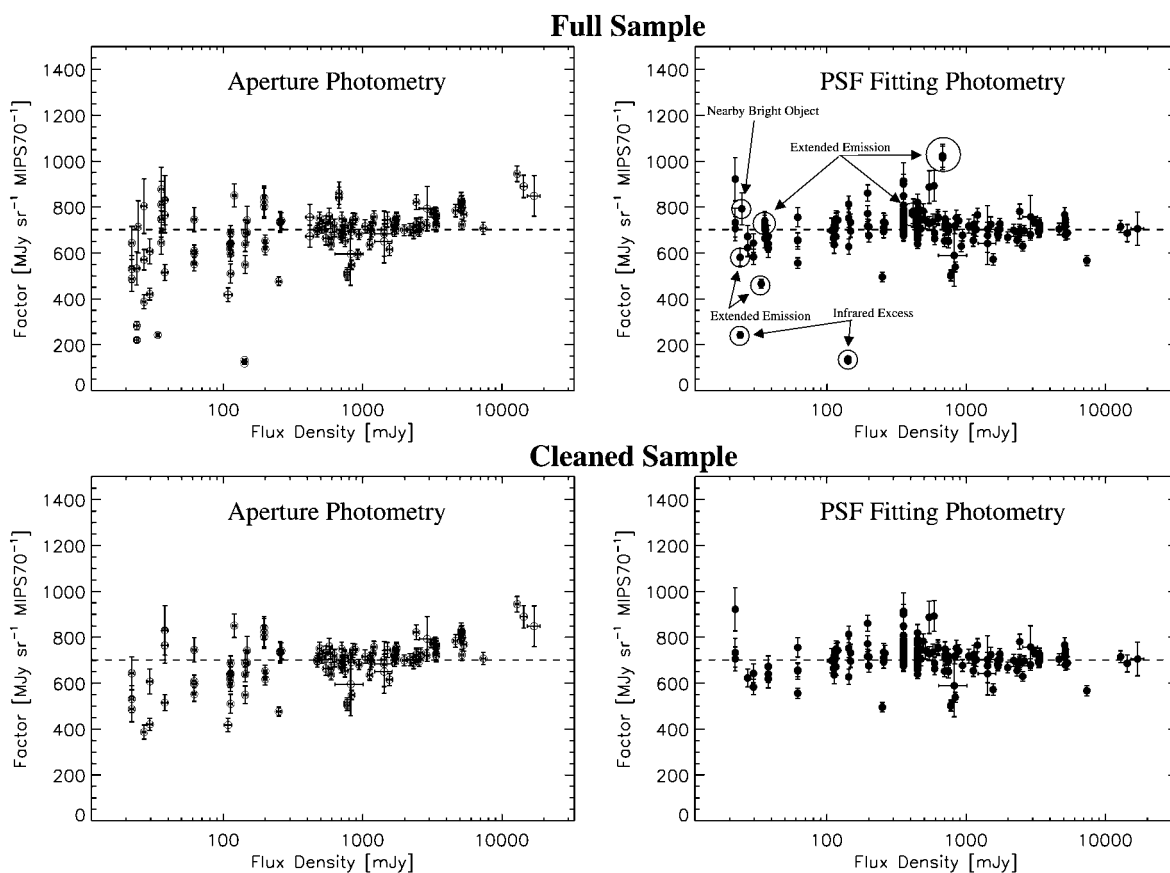**Full Sample**

Cleaned Sample

FIG. 3.—Calibration factor for all the stars with positive flux densities (except for the two repeatability stars) vs. predicted flux density. Each point gives the calibration factor for a single measurement, and thus, a star can have multiple points. The uncertainties on each point include the measurement (y) and flux density prediction (x and y) uncertainties. The dashed line is drawn at the final calibration factor. The cleaned sample is the same as the full sample after the observations that have been rejected are removed. The reasons for rejecting a point are annotated in the upper right panel and discussed in § 3.

density from PSF fitting photometry was normalized to the average flux density of each star and plotted in Figure 6. The sigma-clipped average in 15 bins between 50 and 950 days since launch is also plotted. The dotted vertical lines identify changes in the default dither pattern, bias voltage, and instrument software. This plot clearly shows that the 70 μm array displays measurable long-term variations. The measurements show that the response dropped from the starting value by ~7%

TABLE 6
REJECTED STARS

Name	Reason
HD 36167	Extended emission
HD 35666	Extended emission
HD 42701	Extended emission
HD 141477	Extended emission
HD 166780	Extended emission
HD 169916	Extended emission
HD 173398	Possible infrared excess
HD 173511	Nearby, bright object
HD 173976	Extended emission

around day 200 and then recovered to slightly above the starting value around day 300. After this, the response seems to have stabilized, with evidence for a weak trend downward. While it is tempting to identify the initial variations with the changes in how the data were taken, no clear instrumental parameter has been identified that would cause these variations. Initial testing with other methods of measuring the brightness of these two stars has shown similar but not identical variations. More work is clearly needed to understand the origin of the initial variations.

Even given the initial variations, the repeatability of the two stars is quite good. The repeatabilities for all the measurements are 4.5% for HD 163588 and 3.7% for HD 180711. For reference, the repeatabilities for aperture photometry using the same data are 4.9% for HD 163588 and 3.9% for HD 180711. Given the changes in the operating parameters of the 70 μm array early in the mission, we also computed the repeatabilities using only the data taken after the last change. The repeatabilities for all the measurements after the eighth MIPS campaign are 2.9% for HD 163588 and 2.7% for HD 180711. For reference, the repeatabilities for aperture photometry using the
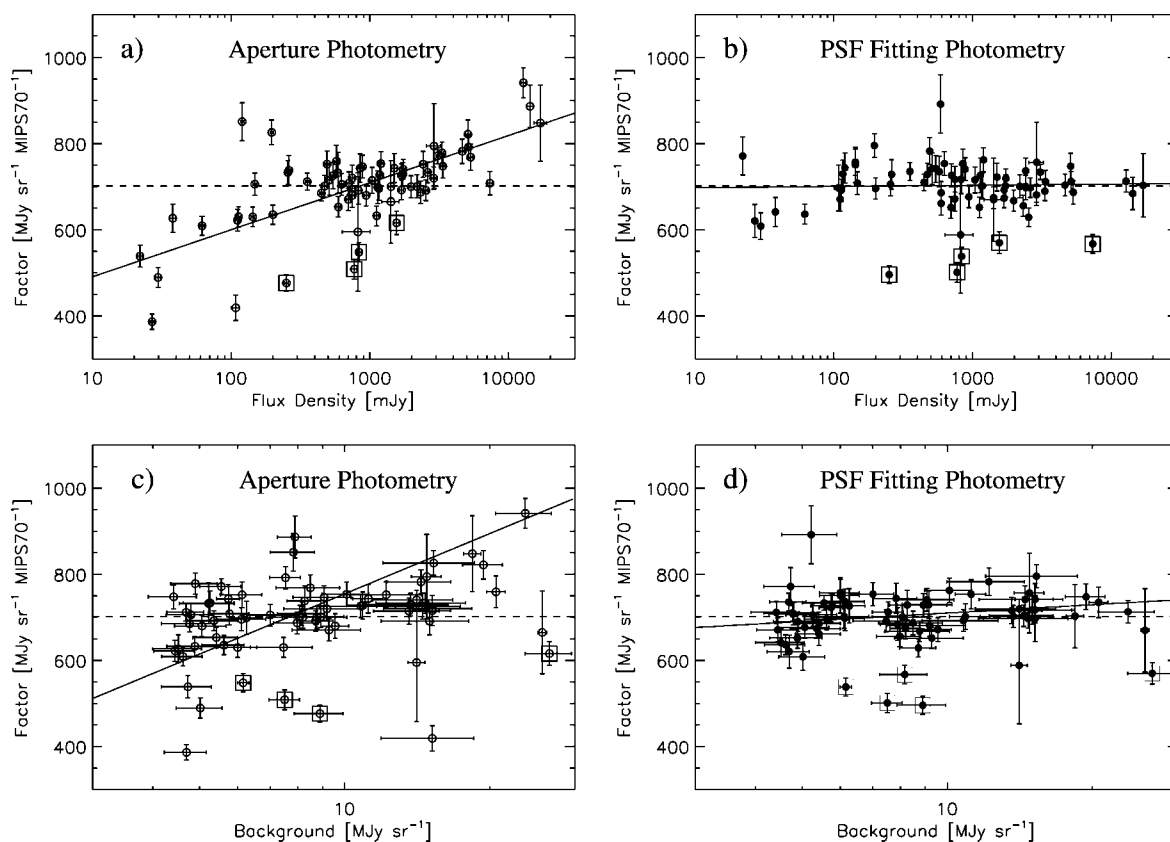
FIG. 4.—Average calibration factor for each star vs. predicted flux density (*a*, *b*) and background (*c*, *d*). The dashed line is drawn at the final calibration factor. The solid line gives the linear fit to all the data except for the five stars with boxes. These stars were rejected from the fit, as they are >5 σ from the mean.

same data are 4.3% for HD 163588 and 3.4% for HD 180711. The combined measurements imply a conservative repeatability of the MIPS 70 μm array of ∼4.5%.
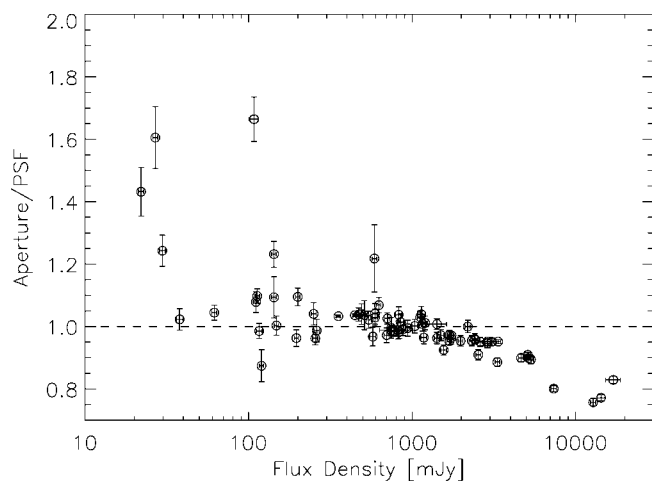
FIG. 5.—Ratio of the aperture to PSF fitting measurements vs. predicted flux density. Each star is represented by a single point, with multiple measurements of a star being averaged before the ratio is computed.

3.3. Time since Anneal

The MIPS 70 μm array is annealed by raising the temperature by a few degrees to remove cosmic-ray damage. This was done every 6 hr until MIPS campaign 20 and every 3–4 hr since then. Residual instrumental signatures are seen to grow with time since anneal, and this change was made to minimize them. In addition to removing cosmic-ray damage, the responsivity of the array is reset (Rieke et al. 2004). The calibration factor should not have a dependence on time since anneal, as all 70 μm measurements are referenced to the internal simulator measurements taken every 2 minutes or less. To check this, Figure 7 shows the calibration factor versus anneal time. No trend is seen.

3.4. Other Checks

The accuracy of the flux density predictions can be checked by comparing the calibration factor derived for stars of different spectral types. The stars in the sample can be divided into three categories: hot stars (B and A dwarfs), solar analogs (early G dwarfs), and cool stars (K and M giants). The weighted average calibration factors (after sigma clipping) for these three categories are 717 ± 8, 717 ± 3, and 701 ± 6 MJy sr^{-1} MIPS70^{-1},
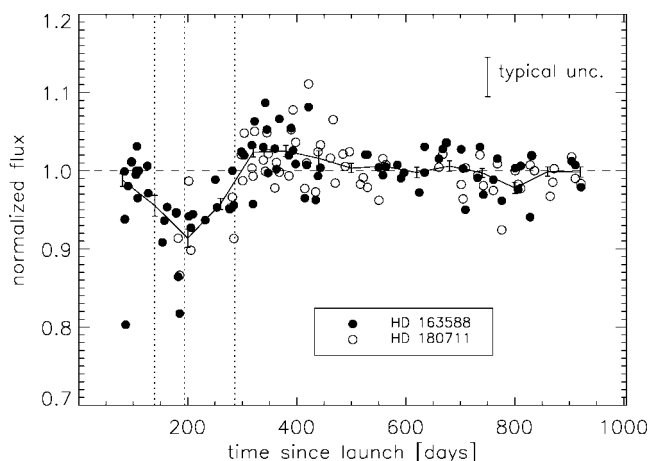
FIG. 6.—Normalized flux densities for the two repeatability stars, HD 163588 and HD 180711, vs. time. The solid line gives the sigma-clipped average in 15 equally spaced bins. The dashed line is drawn at 1. The typical uncertainty of a single measurement is shown in the upper right. The first vertical line indicates the transition between dither patterns (between second and third MIPS campaigns). The second vertical line indicates the transition between array bias voltage values (between fourth and fifth MIPS campaigns). The third vertical line indicates the update to the instrument software (between the eighth and ninth MIPS campaigns).

where the number of measurements contributing to each class are 11, 6, and 58, respectively. None of the averages are significantly different from each other, especially when the small number of measurements contributing to the hot stars and solar analogs is taken into account.

The dependence on exposure time was checked by computing the weighted average calibration factor separately for observations taken with 3.15 and 10.49 s exposures. The resulting calibration factors are 701 ± 6 and 723 ± 7 MJy sr^{-1} MIPS70^{-1} with 62 and 12 measurements contributing to the averages, respectively. As the difference is only 2.4 σ, no significant systematic change with exposure time is seen.

3.5. Noise Characteristics

The behavior of the noise is plotted versus predicted flux density in Figure 8 for the PSF fitting measurements. To compare measurements taken at different exposure times, each noise measurement has been transformed to the equivalent noise in 500 s assuming a $t^{0.5}$ dependence. The noise behavior can be characterized by

$$\sigma(500 \text{ s})^2 = 0.90^2 + [0.20F(\nu)^{0.5}]^2 + [0.0022F(\nu)]^2, \quad (2)$$

where $F(\nu)$ is the predicted 70 μm flux density in mJy. The first term accounts for the confusion noise, the second term the photon noise, and the third term the noise due to the division by the interpolated stimulator flash.

The sensitivity of the MIPS 70 μm band in 500 s can be determined from this fit by computing where the flux is 5 times
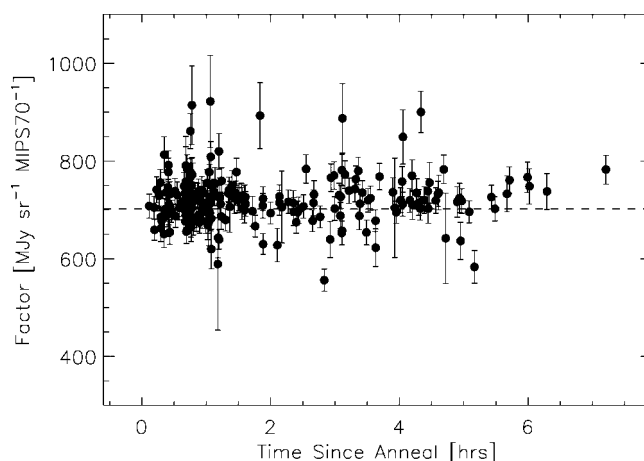
FIG. 7.—Calibration factor vs. time since anneal for all the measurements. The dashed line is drawn at the final calibration factor.

the uncertainty from equation (2). The 5 σ, 500 s sensitivity computed in this fashion is ~5 mJy. This measurement is based on an extrapolation of over a factor of 10 from the lowest measured point and so is fairly uncertain. The sensitivity can be better measured from deep cosmological surveys. The Extragalactic First Look Survey gives a 5 σ, 500 s sensitivity of ~6 mJy after correcting for the updated calibration factor (Frayer et al. 2006a). Somewhat worse sensitivities up to ~8 mJy are seen for other deep MIPS 70 μm cosmological fields (D. Frayer 2006, private communication; C. Papovich 2006, private communication). This sensitivity can include a contribution from confusion, but this is likely to be small, since
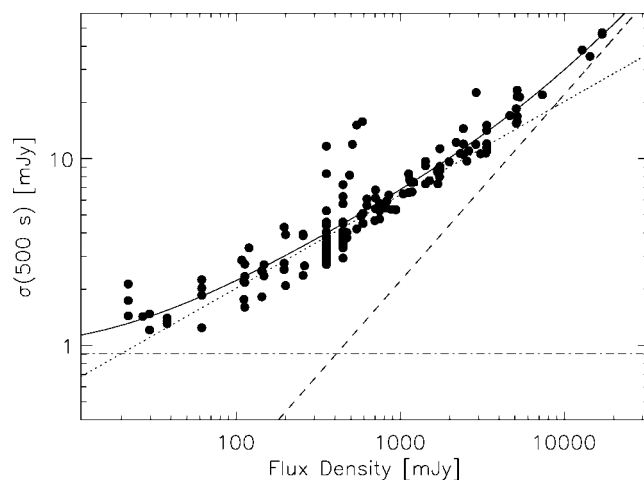

FIG. 8.—Noise vs. predicted flux density for the PSF fitting measurements. Each noise measurement has been converted to the equivalent noise in 500 s assuming that the noise scales as time$^{0.5}$. The solid line gives the fit to the data that is discussed in § 3.5. The dot-dashed line gives the constant term from the fit, the dotted line the term proportional to $F(\nu)^{0.5}$, and the dashed line the term proportional to $F(\nu)$.

the 5 σ confusion noise for MIPS 70 μm coarse-scale observations is estimated at ~1.5–3 mJy (Dole et al. 2004b; Frayer et al. 2006b). Combining the results from the calibration stars and deep cosmological field gives a conservative 5 σ, 500 s sensitivity of 6–8 mJy.

3.6. Coarse-Scale Calibration

The final coarse-scale calibration is based on the PSF fitting results from all the observations (Fig. 4*b*). The final calibration factor of 702 $\pm$ 35 MJy sr^{-1} MIPS70^{-1} was determined by performing a weighted average of the calibration factors measured for each star. There are 66 calibration stars that contribute to this calibration factor. The calibration accuracy is dominated by the 4.5% repeatability uncertainty but also includes contributions from the uncertainty of the mean (very small) and the 2% systematic uncertainty in the 24/70 μm flux density ratios. The conversion directly to flux densities from MIPS70 units implied by the measured calibration factor is 1.60 $\pm$ 0.08 Jy MIPS70^{-1} given that the instrumental flux densities were measured on mosaics with 9.85$''$ $\times$ 9.85$''$ pixels. The calibration factor determined from the 57 stars taken after the ninth MIPS campaign is 696 $\pm$ 34 MJy sr^{-1} MIPS70^{-1}. This shows that the calibration factor is not significantly changed by the variations in the repeatability stars seen prior to the ninth MIPS campaign. The calibration factor determined from the aperture measurements is 704 $\pm$ 35 MJy sr^{-1} MIPS70^{-1}, where only measurements from 0.3 to 1 Jy are used (see Figs. 4 and 5). This shows that the calibrations derived from aperture and PSF fitting measurements are equivalent in the restricted range where the aperture photometry produces accurate results.

An independent analysis of the 70 μm measurements of asteroids (Stansberry et al. 2007) with flux densities $\leq$2 Jy was performed using the standard thermal (STM) and thermophysical (TPM) models fit to the *Infrared Astronomical Satellite* (*IRAS*) and *Infrared Space Observatory* (*ISO*) measurements (T. Muller 2007, private communication). While STM predictions agree within 1% on average with the observations, the TPM predictions are 9% higher on average than the observations. The source and significance of the TPM offset are the subject of further investigation. Nevertheless, the asteroid results confirm the agreement between MIPS, *IRAS*, and *ISO* calibrations within the absolute flux uncertainties. In addition, this indicates that there are no significant differences in the MIPS 70 μm calibration between stars and red sources.

The preliminary calibration factor determined soon after launch was 634 $\pm$ 127 MJy sr^{-1} MIPS70^{-1}. The new value is 11% larger than this preliminary value, well within the 20% uncertainty in the preliminary value. This 11% change is not unexpected given that the preliminary value was based on a handful of measurements of a single star and the data reduction at the time did not include the extra steps to correct residual instrumental signatures. Existing data can be corrected to the new calibration factor by multiplying by the ratio of the new

to old calibration factors. Note that the calibration factor applied to data reduced using the SSC pipeline is given by the FITS header keyword FLUXCONV.

The coarse-scale calibration factor is determined from photometry mode observations but should apply directly to scan map mode observations, as both modes share the same optical train and only differ in the dithering strategy. The relative response between the scan map and coarse-scale photometry mode has been checked by observing the same source in both modes. It was found that the same flux density was measured within the uncertainties.

The consistency of the 70 μm calibration with the 24 μm calibration was checked using stars that were observed at both 24 and 70 μm. There are 36 such measurements for stars with 24 μm flux densities below 4 Jy (24 μm saturation limit). The resulting sigma-clipped average of the ratio of the observed to model 24/70 color ratio is 1.002 $\pm$ 0.013, showing that the 24 and 70 μm calibrations are consistent.

3.7. Extended versus Point-Source Calibration Check

The calibration factor determined above was calculated from observations and predictions of point sources. Given the complex response of Ge:Ga detectors to sources with different spatial extents, it is important to verify that the point-source calibration applies to extended sources. This can be checked by comparing the total fluxes of resolved galaxies measured at 70 μm to those predicted by *IRAS* (Beichman et al. 1988) measurements at 60 and 100 μm. Galaxies provide good objects for such a check, as they are discrete extended sources that were well measured by *IRAS* and have a significant component of their flux that is resolved by MIPS at 70 μm.

The galaxy fluxes are compared using the 75 *Spitzer* Infrared Nearby Galaxies Survey (SINGS; Kennicutt et al. 2003) galaxies from global measurements given by Dale et al. (2005) and updated by Dale et al. (2007). This sample is supplemented at the highest flux densities with global measurements of M31 (Gordon et al. 2006), M33 (Hinz et al. 2004), M101 (K. D. Gordon et al. 2007, in preparation), and the Large Magellanic Cloud (LMC; Meixner et al. 2006). The predictions of the 70 μm flux densities from the *IRAS* 60 and 100 μm measurements were done by first color correcting the *IRAS* measurements using the measured 60/100 flux density ratio to pick the appropriate power-law color correction (Beichman et al. 1988) and then interpolating to the effective wavelength of the MIPS 70 μm band of 71.42 μm. The average color corrections were 1.0 for both *IRAS* 60 and 100 bands. The MIPS 70 μm measurements were corrected to the updated calibration factor and color corrected using the correction for the same power law determined for the *IRAS* measurements (Stansberry et al. 2007). The average MIPS 70 μm color correction was 0.93. Figure 9 gives the ratio of the MIPS to predicted *IRAS* 70 μm flux densities for all the galaxies with flux densities above 1 Jy. The weighted average of this ratio is 0.99, which is well within
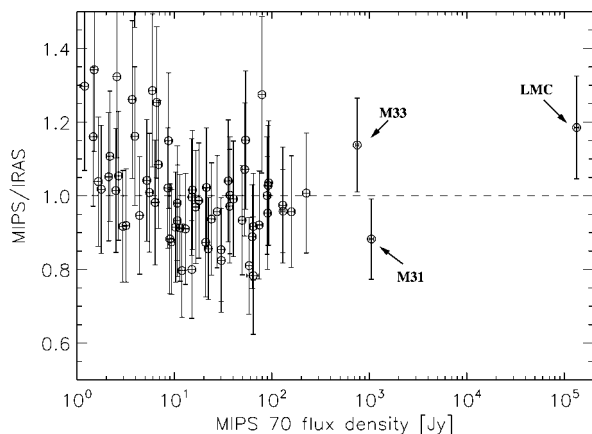
FIG. 9.—Ratio of MIPS 70 μm measured flux density to the 70 μm flux density predicted from *IRAS* 60 and 100 μm measurements shown as a check of the extended source calibration. The sample shown is comprised of the 75 SINGS galaxies supplemented by the LMC, M31, M33, and M101. The uncertainties are computed from the uncertainties in the *IRAS* and MIPS measurements. The dashed line is drawn at a value of 1.
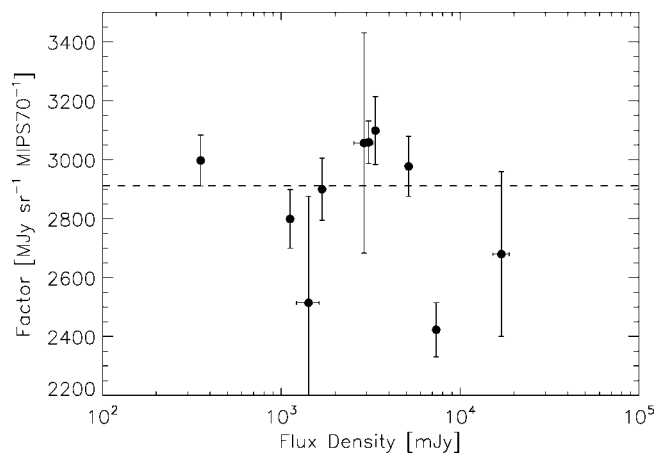

FIG. 10.—Fine-scale calibration factor vs. predicted flux density. The multiple measurements of each star have been averaged, and the plotted uncertainty includes the flux density prediction uncertainty. The final calibration factor is shown as a dashed line.

the uncertainties on the absolute calibration of MIPS 70 μm (5%) and *IRAS* 60 μm (5%; Beichman et al. 1988). This shows that the MIPS 70 μm point-source calibration applies for extended sources. This comparison also serves as another check that the photometry and scan observing modes share the same calibration even though the calibration factor is derived from photometry mode observations while the galaxies were observed with the scan map mode.

3.8. Fine-Scale Calibration

The fine-scale calibration should be similar to the coarse-scale calibration modulo the different pixel scales (5.24″ pixel^{-1} instead of 9.85″ pixel^{-1}) and optical trains. Figure 10 shows the calibration factor for PSF fitting photometry. The fine-scale calibration factor determined from these data is 2894 $\pm$ 294 MJy sr^{-1} MIPS70F^{-1}. The conversion directly to flux densities from MIPS70F units implied by this calibration factor is 1.87 $\pm$ 0.188 Jy MIPS70^{-1} given that the instrumental flux densities were measured on mosaics with 5.24″ $\times$ 5.24″ pixels. The fine-scale calibration factor is 4.12 times the coarse-scale factor. This is larger than the ratio of pixel areas (3.53), implying that the different optical train has a significant effect on the calibration. Only 10 calibration stars are used for the fine-scale calibration, and, as a result, the fine-scale calibration must be taken as preliminary. The uncertainty on the fine-scale calibration is formally only 5%, but we have doubled this to account for the small sample used. In general, the fine-scale mode should be used for probing structure and the coarse-scale used when accurate photometry is needed.

3.9. Comparison to Previous Missions

The repeatability, absolute calibration accuracy, and sensitivity of the coarse-scale MIPS 70 μm band can be compared to those of previous missions. Imaging of point sources in bands similar to the MIPS 70 μm band has been provided in the past by the *IRAS* and *ISO* (Kessler et al. 1996).

IRAS 60 μm photometry of point sources has a repeatability of 11% and an absolute calibration uncertainty of 5% (Beichman et al. 1988). The *IRAS* Faint Source Catalog (Moshir et al. 1992) is 94% complete at 0.2 Jy. The almost full sky coverage of *IRAS* allows for a comparison of the *IRAS* 60 μm and MIPS 70 μm fluxes. There are 30 stars with both MIPS 70 μm and *IRAS* 60 μm Faint Source Catalog measurements (Moshir et al. 1990) and *IRAS* 60 μm fluxes above 0.6 Jy. The average ratio of the *IRAS* 60 μm to MIPS 70 μm flux densities is 1.35 $\pm$ 0.01, and the expected ratio from a Rayleigh-Jeans model is 1.42. Thus, the *IRAS* 60 μm flux densities need to be multiplied by 1.05 in order to put them on the G. H. Rieke et al. (2007, in preparation) system.

The ISOPHOT instrument (Laureijs et al. 2003) included a 70 μm band with the P3 detector and a 60 μm band with the C100 detector. The P3 reproducibility was 10%–20% and absolute accuracy was 7%. The C100 repeatability was 3%–20% and absolute accuracy was 15%–25% (Klaas et al. 2003). The sensitivity of ISOPHOT in these bands is approximately 7.5–20 mJy 1 σ in 256 s (Laureijs et al. 2003), which corresponded to a 5 σ, 500 s sensitivity of 30–70 mJy. This sensitivity is better than that found from the 95 μm deep-field observations of Rodighiero et al. (2003), where the 3 σ, 5184 s sensitivity is 16 mJy, which corresponds to a 5 σ, 500 s sensitivity of 86 mJy.

The MIPS 70 μm observations compare favorably, with bet-

ter repeatability (4.5%), as good or better absolute calibration uncertainty (5%), and higher sensitivity (6–8 mJy 5 σ, 500 s) than previous missions imaging in similar bands. This is to be expected, as the MIPS 70 μm detector operation has benefited from lessons learned from past missions.

4. SUMMARY

The calibration of the MIPS 70 μm coarse- and fine-scale imaging modes was determined from many observations taken over the first 2.5 yr of the *Spitzer* mission.

1. The characterization and calibration of the MIPS 70 μm coarse-scale mode was determined from measurements of 78 stars of spectral types B–M, with flux densities from 22 mJy to 17 Jy, and on backgrounds of 4–26 MJy sr^{-1}. The coarse-scale calibration factor is 702 $\pm$ 35 MJy sr^{-1} MIPS70^{-1} and was determined from measurements of 66 stars. A handful of stars were rejected due to possible infrared excesses, contamination from nearby extended emission, and nearby very bright sources.

2. Accurate photometry of point sources in coarse-scale mode requires two simple processing steps beyond the standard data reduction to remove long-term detector transients.

3. PSF fitting photometry is seen to produce better measurements than aperture photometry due to better handling of nearby stars and background structure and less weighting of the PSF core where flux nonlinearities have a larger effect.

4. Using PSF fitting photometry, no significant trends in calibration factor versus predicted flux density, predicted background, exposure time, spectral type, and time since anneal were found.

5. The photometric repeatability is 4.5% measured from two stars observed during every campaign and includes variations on all timescales probed.

6. The 5 σ, 500 s sensitivity of coarse-scale observations is 6–8 mJy and was determined from the calibration stars and deep cosmological surveys.

7. The applicability of the coarse-scale calibration factor, derived from point-source observations, to extended sources was confirmed using a sample of galaxies observed with MIPS and *IRAS*.

8. The preliminary fine-scale calibration factor is 2894 $\pm$ 294 MJy sr^{-1} MIPS70F^{-1} and was determined from measurements of 10 stars with flux densities from 350 mJy to 17 Jy.

REFERENCES

Beichman, C. A., Neugebauer, G., Habing, H. J., Clegg, P. E., & Chester, T. J. 1988, *Infrared Astronomical Satellite* (*IRAS*) Catalogs and Atlases, Vol. 1, Explanatory Supplement (Washington, DC: GPO)
Bryden, G., et al. 2006, ApJ, 636, 1098
Calzetti, D., et al. 2005, ApJ, 633, 871
Dale, D. A., et al. 2005, ApJ, 633, 857
———. 2007, ApJ, 655, 863
Diolaiti, E., et al. 2000, A&AS, 147, 335
Dole, H., et al. 2004a, ApJS, 154, 87
———. 2004b, ApJS, 154, 93
Engelbracht, C. W., et al. 2007, PASP, 119, 994
Frayer, D. T., et al. 2006a, AJ, 131, 250
———. 2006b, ApJ, 647, L9
Gordon, K. D., et al. 2005, PASP, 117, 503
———. 2006, ApJ, 638, L87
Haegel, N. M., et al. 2001, Appl. Opt., 40, 5748
Hinz, J. L., et al. 2004, ApJS, 154, 259
Kennicutt, R. C., Jr., et al. 2003, PASP, 115, 928
Kessler, M. F., et al. 1996, A&A, 315, L27

Kim, J. S., et al. 2005, ApJ, 632, 659
Kirby, D. J., Rieke, G. H., & Lebofsky, L. A. 1994, AJ, 107, 2226
Klaas, U., et al. 2003, in The Calibration Legacy of the *ISO* Mission, ed. L. Metcalfe et al. (ESA SP-481; Noordwijk: ESA), 19
Krist, J. 2002, Tiny Tim/*SIRTF* User's Guide (Pasadena: SSC)
Kurucz, R. L. 1979, ApJS, 40, 1
Laureijs, R. J., Klaas, U., Richards, P. J., Schulz, B., & Abraham, P. 2003, The *ISO* Handbook, Vol. IV, PHT—The Imaging Photo-Polarimeter (ESA SP-1262; Noordwijk: ESA)
Meixner, M., et al. 2006, AJ, 132, 2268
Moshir, M., Kopman, G., & Conrow, T. A. O. 1992, *IRAS* Faint Source Survey, Explanatory Supplement, version 2 (Pasadena: IPAC)
Moshir, M., et al. 1990, *IRAS* Faint Source Catalogue, version 2.0 (Greenbelt: NASA)
Rieke, G. H., et al. 2004, ApJS, 154, 25
Rodighiero, G., et al. 2003, MNRAS, 343, 1155
Stansberry, J., et al. 2007, PASP, 119, 1038
Werner, M. W., et al. 2004, ApJS, 154, 1
Young, E. T., et al. 1998, Proc. SPIE, 3354, 57